Tomographic inversion of *Pn* travel times in China

Chuntao Liang and Xiaodong Song[1]
Department of Geology, University of Illinois at Urbana-Champaign, Urbana, Illinois, USA

Jinli Huang
Center of Analysis and Prediction, China Seismological Bureau, Beijing, China

Received 8 September 2003; revised 13 August 2004; accepted 24 August 2004; published 9 November 2004.

[1] *Pn* travel times are useful for studying crustal and uppermost mantle structure and regional tectonics because they are affected by crustal velocity and thickness as well as uppermost mantle velocity and anisotropy. We obtained 57,740 *Pn* travel time picks from 5433 earthquakes and 307 stations from Chinese national and provincial earthquake bulletins and the International Seismological Center bulletins to invert for *Pn* velocity variation and anisotropy and station delays in China. Our inversion reveals significant features that correlate with surface geology. The main results are as follows: (1) The *Pn* velocities show a mosaic of very fast and very slow anomalies, mirroring the heterogeneous geology of China at the surface. The *Pn* velocities are high beneath the major basins in the west (Sichuan, Qaidam, west Tarim, Tulufan, and Junggar) and low in areas of active volcanoes (Myanmar and western Yunnan) and Quaternary volcanism in northern Tibet, in seismically active areas in north China and Tien Shan, and in the southern part of south China (the Hainan plume). (2) The *Pn* anisotropy beneath the major basins in the west is generally weak. Strong anisotropy is found beneath high-deformation regions (the Tibetan Plateau, southeastern margin of the Tibetan Plateau, western Tien Shan, and part of north China), suggesting the anisotropy is likely related to recent large-scale tectonic activity. (3) A large area of north China shows prominent low *Pn* velocity beneath Archean basement with thin crust. Our observations are consistent with rifting, lithospheric thinning, and mantle upwelling in the region. The *Pn* anisotropy is consistent with a dextral simple shear in the NNE direction in the lithosphere mantle during the last (and ongoing) major deformation period. (4) The *Pn* velocity in northern Tibet is generally lower than that in the south. Southern Tibet has significant E-W structure. Low-velocity anomalies can be traced from northern Tibet across southwestern Tibet and south central Tibet to near the India plate. Anisotropy is absent beneath much of the Himalaya block, but consistent anisotropy with E-W fast direction is present beneath the Lhasa block and large anisotropy (up to 4%) is observed in low-velocity regions of the northern and western Tibet. Complex station delays in the eastern margin of the plateau suggest that the whole crust may be highly deformed. The anisotropy pattern in the southeastern margin of the Tibetan Plateau suggests a mantle lithospheric deformation similar to the clockwise rotation of material observed at the surface. (5) Crustal thicknesses inferred from our station delays are consistent with previous models, which correlate well with surface topography. *INDEX TERMS:* 7205 Seismology: Continental crust (1242); 7218 Seismology: Lithosphere and upper mantle; 8110 Tectonophysics: Continental tectonics—general (0905); 8180 Tectonophysics: Tomography; *KEYWORDS: Pn*, tomography, China

Citation: Liang, C., X. Song, and J. Huang (2004), Tomographic inversion of *Pn* travel times in China, *J. Geophys. Res.*, *109*, B11304, doi:10.1029/2003JB002789.

1. Introduction

[2] China is geologically highly heterogeneous, consisting of Precambrian platforms surrounded by accreted continental fragments and fold belts of various ages (Figure 1). The heterogeneity is most striking with the sharp contrast between the Tibetan Plateau in the west with an average elevation of 5000 m related to the India-Eurasia collision about 60 Myr ago and the Archean core of the Sino-Korean

[1]Also at Center of Analysis and Prediction, China Seismological Bureau, Beijing, China.

0148-0227/04/2003JB002789$09.00

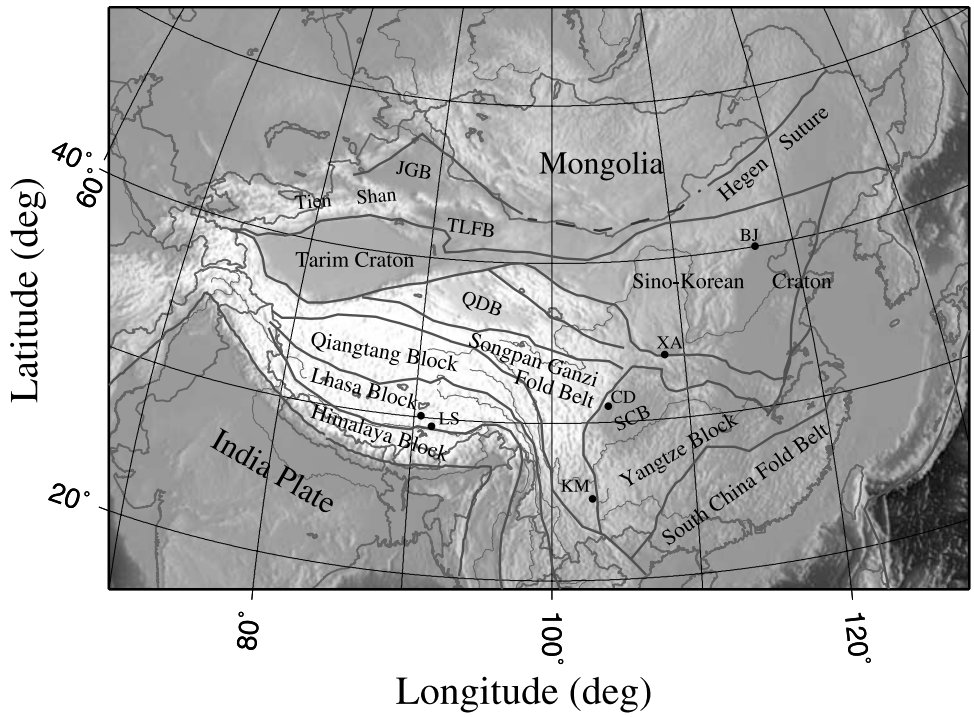

Figure 1. Major crustal elements of China (modified from *Zhang et al.* [1984]). Abbreviations are Junggar Basin (JGB), QDB (Qaidam Basin), SCB (Sichuan Basin), TLFB (Tulufan Basin), BJ (Beijing), XA (Xi'an), CD (Chengdu), KM (Kunming), and LS (Lasa).

and Yangtsz cratons in the east (Figure 1). The country is seismically very active, even in densely populated areas, such as Sichuan, Yunnan provinces in southwestern China and in the Beijing-Tianjing-Tangshan area in northern China. Thus studies of crustal and upper mantle structure beneath China are of major interests over the years in understanding the tectonics of the region and have important implications for earthquake hazards.

[3] Most of the seismological studies in the western countries have focused on the Tibetan Plateau and Tien Shan region and have relied upon a few stations from global data sets, including the World-Wide Seismograph Station Network stations adjacent to China and sparse Chinese Digital Seismic Network (CDSN) with 10 stations established in 1986 by agencies of the United States and China. These studies include surface wave inversions [e.g., *Chen and Molnar*, 1975; *Patton*, 1980; *Bourjot and Romanowicz*, 1992; *Zhang and Lay*, 1996; *Wu et al.*, 1997; *Ritzwoller and Levshin*, 1998; *Curtis et al.*, 1998; *Griot et al.*, 1998; *Mahdi and Pavlis*, 1998; *Lebedev and Nolet*, 2003] and body wave travel time and waveform studies [e.g., *Ni and Barazangi*, 1983; *Lyon-Caen*, 1986; *Zhao et al.*, 1991; *Roecker et al.*, 1993; *Beckers et al.*, 1994; *Chen et al.*, 1997; *Bump and Sheehan*, 1998; *Wolfe and Vernon*, 1998; *Hartse et al.*, 1997; *Rapine et al.*, 1997; *Zhu et al.*, 1997; *Fan and Lay*, 1998; *Phillips et al.*, 1998; *Chen and Ozalaybey*, 1998; *Xie and Patton*, 1999; *Phillips et al.*, 2000]. The data coverages are generally poor under China. In recent years, a number of large projects have been carried out using temporary stations, which focused on selected areas in Tibet or Tien Shan, such as the multinational International Deep Seismic Sounding of Tibet and Himalayas (INDEPTH) project [e.g., *Nelson et al.*, 1996].

[4] Global tomographic inversions have yielded important results in the region; for example, *van der Hilst et al.* [1997] and *Grand et al.* [1997] showed the signature of the subducted slab of the Mesozoic Tethys sea into the deep mantle. Many high-resolution tomographic studies of the region using regional and local travel time or surface dispersion data have been carried out inside China [e.g., *Liu et al.*, 1990; *Liu and Jin*, 1993; *Xu et al.*, 2000; *Xu et al.*, 2001; *Zhu et al.*, 2002; *Lei et al.*, 2002; *Huang et al.*, 2002; *Xu et al.*, 2002; *Huang et al.*, 2003a] with most published in the Chinese literature. Over the decades, one of the most significant efforts carried out in China was deep seismic sounding (DSS) using active sources to image the crustal structure. More than 36,000 km of DSS profiles have been acquired in China since 1958 [*Li and Mooney*, 1998]. They conclude that the upper mantle *Pn* velocities are about 8.0 ± 0.2 km/s beneath China and the average crust thickness becomes progressively thicker from the east to west with the thickness of more than 70 km beneath the Tibetan Plateau.

[5] In this study, we use the travel times of *Pn* waves to invert for the velocity and anisotropy distribution in the uppermost mantle and the crustal thickness of China. A *Pn* wave can be regarded as a head wave traveling below the Moho along the top of the upper mantle (Figure 2). Crustal thickness and *Pn* velocity are basic parameters of the Earth's interior. *Pn* arrival times are routinely used for locating regional events, thus accurate *Pn* velocity models are important for earthquake location. *Pn* velocity varies with changes in temperature and material composition and *Pn* anisotropy may indicate the history of mantle deformation [e.g., *Bamford*, 1977; *Hearn*, 1996]. Thus *Pn* velocity and anisotropy has also become an important tool to probe lithospheric structure and dynamics [e.g., *Hearn*, 1996;

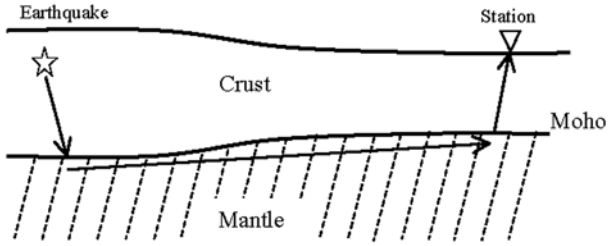

Figure 2. Schematic diagram of *Pn* wave propagation. The *P* wave is critically refracted at the Moho boundary. The ray path has three segments, associated with the source, the receiver, and the mantle. Our tomographic inversion solves for the static delay times in the crust associated with the earthquake and the station and the lateral velocity variation and the velocity anisotropy at the top the mantle encountered by the mantle segment of the ray path.

Silver, 1996]. Some *Pn* inversions haven been conducted in local regions of China, such as the Tibetan Plateau [*Zhao and Xie*, 1993; *McNamara et al.*, 1997], Xinjiang (western China) [*Pei et al.*, 2002], and southwest China [*Huang et al.*, 2003b], and in the whole country [*Wang et al.*, 2002; *Sun et al.*, 2004]. Here we use *Pn* arrival time data from the *Annual Bulletin of Chinese Earthquakes* (ABCE) (a national earthquake catalog compiled by the Institute of Geophysics, China Seismological Bureau), two provincial earthquake bulletins, as well as the International Seismological Center (ISC) bulletins. The large collection of data allows us to adopt stricter criteria on data selection to obtain high-quality data as well as good ray coverage. The tomographic inversion provides a survey of the large-scale structure of the *Pn* velocity, its lateral variation and anisotropy, and the crustal thickness of China. The model reveals significant features that may have implication for the structure and tectonics of the region.

[6] The tectonics of China and surrounding areas are complex and challenging. We give a brief summary of the tectonic history of China below, following a few past reviews [*Zhang et al.*, 1984; *Li*, 1998; *Wang and Mo*, 1995; *Burchfiel and Royden*, 1991; *Yin and Harrison*, 2000]. China is principally a part of the Eurasian plate, except for the Himalayas and the Coastal Range of Taiwan, which are margins of the Indian and Philippine Sea plates, respectively. It consists of nuclei of Precambrian cratons and a mosaic of later accreted microcontinents and fold belts. The fold belts and ancient suture zones are characterized by widespread ophiolite, blueshist, and mélange belts. There are three major Precambrian cratons: the Sino-Korea craton, also known as the North China Block (NCB), the Tarim craton, and the Yangtze craton. The combination of the Yangtze craton and the Precambrian Cathaysia Block, which consists of a part in the south China Fold belt and a part underwater to the east, is also called as South China Block (SCB).

[7] The Tarim-Sino-Korea paleocontinent accreted to the Angaraian paleoplate (with Siberia craton as nucleus) in the north by consuming the oceanic crust between them. The two continents collided along the Junggar-Hegen suture in the Permian (250–280 Ma). Both the NCB and the SCB were parts of the supercontinent Rodinia in the early Neoproterozoic (at 1.0 Ga). The breakup of Rodinia separated the NCB and the SCB from the other former Rodinian continents. The collision between the NCB and SCB started at about the same time as the north China-Angaraian collision in the Permian. Major suturing between the two blocks occurred during the late Middle Triassic to Middle Jurassic along the Sulu and Qinling-Dabie orogens, which led to the formation and exhumation of ultrahigh-pressure rocks in both regions.

[8] Two major processes controlled the Cenozoic tectonics of East Asia: (1) the collision of the India and Eurasia plates that started at about 40–70 Ma [*Molnar et al.*, 1993; *Rowley*, 1996; *Yin and Harrison*, 2000]; and (2) the subduction of the Pacific (and later the Philippine Sea) plate that started during the late Mesozoic. The continued subduction of the Pacific and Philippine Sea oceanic crust led to the opening of the Japan Sea and the formations of the Western Pacific archipelagos.

[9] The India-Eurasia collision may have controlled most of the large-scale Cenozoic tectonic history of Asia [e.g., *Molnar and Tapponnier*, 1975; *Tapponnier et al.*, 1982]. The Himalayan-Tibetan orogen was built upon a complex tectonic assemblage of microcontinents, flysch complexes, and island arcs accreted onto the southern margin of Eurasia since the early Paleozoic. The India-Eurasia collision caused the formation of the Himalayas, thickening of the Tibetan crust, and the uplift of the Tibetan Plateau. At least 1400 km of north-south shortening has been absorbed by the orogen since the onset of the collision [*Yin and Harrison*, 2000].

[10] During Cenozoic times, extension occurred along much of the eastern margin of Asia, from Java and Summatra in the south to the Sea of Japan in the north. It is thought that the India-Eurasia collision forced the extrusion of continental blocks eastward along large strike-slip faults, causing the extension in the eastern margin of Asia and the opening of the South China Sea [e.g., *Molnar and Tapponnier*, 1975; *Tapponnier et al.*, 1982]. This, however, is uncertain. Numerical simulation of the collision with Asia as a viscous sheet deformed by a rigid indenter (India) suggests no extrusion beyond the thickened Tibetan Plateau and thus other tectonic features east of the plateau may not be related to the collision [e.g., *England and Houseman*, 1986; *Royden et al.*, 1997]. Furthermore, it is argued that the extension in the eastern margin is related to the interactions between Eurasia and the oceanic plates to the east [*Burchfiel and Royden*, 1991; *Northrup et al.*, 1995].

2. Inversion Method

[11] We follow the basic inversion scheme of *Pn* waves by *Hearn* [1996]. The *Pn* travel time is the sum of the travel time in the crust from the source to the Moho and from the Moho to the receiver, and the travel time of the head wave traveling at the top of the upper mantle (Figure 2). We divide the study area into two-dimensional (2-D) cells of 0.5° by 0.5° along the longitudes and latitudes. Thus the *Pn* travel time residual (the observed travel time minus the predicted travel time for a reference model) can be written

$$\Delta t_{ij} = \Delta t_i^{eq} + \Delta t_j^{st} + \sum_{k=1}^{N} d_{ijk}\Delta s_k + \sum_{k=1}^{N} d_{ijk}\cos\left(2\phi_{ijk}\right)a_k + \sum_{k=1}^{N} d_{ijk}\sin\left(2\phi_{ijk}\right)b_k, \quad (1)$$

where t_{ij} is the travel time from the ith earthquake to the jth station; t_i^{eq} and t_j^{st} are the travel times from the ith earthquake to the Moho and from the Moho to the jth station, respectively. The earthquake delay Δt_i^{eq} and the station delay Δt_j^{st} represent the discrepancy between the actual travel time and the predicted travel time in the crust, which comes from the departure of the crustal velocity or the crustal thickness or both from the reference model; the earthquake delay Δt_i^{eq} is also affected by errors in earthquake depth. The travel time perturbation in the upper mantle is separated into contribution from the velocity (slowness) perturbation ($\sum_{k=1}^{N} d_{ijk}\Delta s_k$) and contribution from anisotropy ($\sum_{k=1}^{N} d_{ijk}\cos(2\phi_{ijk})a_k + \sum_{k=1}^{N} d_{ijk}\sin(2\phi_{ijk})b_k$), where d_{ijk} is the length of the ray from the ith earthquake to the jth station in the kth cell of the mantle (d_{ijk} is 0 if the ray ij does not pass cell k), s_k is the slowness (1/velocity) of the kth cell, and the a_k and b_k are the anisotropy parameters in the kth cell; the ϕ_{ijk} is the azimuth of the ray from the ith earthquake to the jth station at cell k; and N is the total number of cells. Here we assume the form of transverse anisotropy for *Pn* waves, which can be described by a sinusoidal 2ϕ azimuthal variation [*Backus*, 1965]. Note that we use the azimuth of the ray at each cell (ϕ_{ijk}) instead of the same azimuth (or back azimuth) of the ray for all cells along the ray [*Hearn*, 1996], because the azimuth (back azimuth) may change substantially along the ray. The magnitude of anisotropy at cell k is given by $(a_k^2 + b_k^2)^{1/2}$ and the direction of fastest wave propagation is given by arctan $(b_k/a_k)/2$ from the north.

[12] The linear system of equations (1) can be written in matrix form:

$$\mathbf{d} = \mathbf{G}\mathbf{m}, \tag{2}$$

where $\mathbf{d}$ is the data vector whose elements are the observed residuals of rays Δt_{ij}, and the number of the elements is equal to the number of rays; the solution vector $\mathbf{m}$ comprises all the model parameters we want to solve: earthquake and station delays (Δt_i^{eq} and Δt_j^{st}), and *Pn* slowness perturbation Δs_k and anisotropy parameters a_k and b_k in every cell; the matrix $\mathbf{G}$ is called the data kernel, which relates the data (observed residuals) and the model parameters and depends on the ray coverage. The matrix $\mathbf{G}$ is large and sparse (with a large number of elements being zero). Thus our *Pn* inversion problem is equivalent to solving a large sparse linear sparse equation system.

[13] Methods used to solve the linear system such as equation (2) are widely discussed by many authors [e.g., *Nolet*, 1987]. In this study, we use a preconditioned version of the LSQR algorithm [*Paige and Saunders*, 1982a, 1982b]. A preconditioning matrix $\mathbf{P}$ is applied to (2) to obtain an equivalent system:

$$\mathbf{G}'\mathbf{m}' = \mathbf{d}, \tag{3}$$

where $\mathbf{G}' = \mathbf{G}\mathbf{P}$, $\mathbf{m}' = \mathbf{P}^{-1}\mathbf{m}$. The LSQR iteratively finds the least squares solution for $\mathbf{m}'$ and the final solution $\mathbf{m} = \mathbf{P}\mathbf{m}'$. The preconditioning does not change the least squares norm of the solution, but it accelerates the convergence rate [*Paige and Saunders*, 1982a, 1982b].

[14] Preconditioning is needed because the elements of matrix $\mathbf{G}$ in equation (2) for slowness and anisotropy are the ray lengths in kilometers, which are 2 orders of magnitude of the matrix elements (which are 1) for station and event delays. Any nonsingular matrix $\mathbf{P}$ that approximates the inverse to $\mathbf{G}$ can be used as a preconditioner. We choose a preconditioning matrix $\mathbf{P}$ below, which is similar to the one used by *Hearn and Ni* [1994]. The matrix makes $\mathbf{G}$ dimensionless and takes into account ray path density of each station, event, and cell.

$$\mathbf{P}_{N_x \times N_x} = \begin{bmatrix} \mathbf{P}^c_{N_{3c} \times N_{3c}} & & \\ & \mathbf{P}^{st}_{N_{st} \times N_{st}} & \\ & & \mathbf{P}^{eq}_{N_{eq} \times N_{eq}} \end{bmatrix}, \tag{4}$$

where $\mathbf{P}^c$, $\mathbf{P}^{st}$, and $\mathbf{P}^{eq}$ are diagonal matrices with the dimensions equal to three times the number of cells (N_{3c}), the number of the stations (N_{st}), and the number of earthquakes (N_{eq}), respectively. The diagonal elements for $\mathbf{P}^c$ is given by $1/\sqrt{\sum D_i d_i}$, where D_i is the total ray path length for ray i, and d_i is the length of ray i within the corresponding cell, the sum is over all rays crossing the cell. The diagonal elements for $\mathbf{P}^{st}$ or $\mathbf{P}^{eq}$ are given by $1/\sqrt{N_r}$, where N_r are the number of rays associated with the corresponding station or earthquake. The dimension of matrix $\mathbf{P}$ is equal to the total number of inversion parameters, i.e., $N_x = N_{3c} + N_{st} + N_{eq}$.

[15] Because of uneven distribution of ray paths and data errors, the linear system (2) or (3) is generally highly ill-conditioned, which may result in singularities with extremely high or low values in local areas and make the inversion unstable. A common approach in dealing with the problem is to impose additional constraints to regularize the solutions [*Van Der Sluis and Van Der Vorst*, 1987]. Here we impose the smoothness constraints as described by *Lees and Crosson* [1989]. Because our slowness solution is a discrete version of the continuously varying field, it is desirable to have some constraints for our solutions to have a certain measure of roughness. Smoothed solutions also allow us to concentrate on more coherent large-wavelength structures and ignore local small-scale variations in interpreting inversion results.

[16] The smoothness constraints are imposed by minimizing the Laplacian (second derivative) of the solutions $\mathbf{m}'$ (instead of $\mathbf{m}$). Thus our LSQR solutions minimize the following damped least squares functional: $\|\mathbf{G}'\mathbf{m}' - \mathbf{d}\|^2 + \lambda^2\|Lx\|^2$. Here $\|\mathbf{v}\|$ denotes the Euclidean (L_2) norm with $\|\mathbf{v}\|_2 = (\mathbf{v}^T\mathbf{v})^{1/2}$, and the Laplacian operator L is applied to the component $\boldsymbol{x}$ of $\mathbf{m}'$ that corresponds to slowness or either anisotropic coefficient. The parameter λ controls the level of smoothing, which trades off with the misft (error reduction) $\|\mathbf{G}'\mathbf{m}' - \mathbf{d}\|$. As λ increases, the inversion image becomes smoother and the misfit increases. We choose λ = 0.3 in this study.

3. Data and Model Resolution

[17] Our *Pn* arrival time picks are from the Chinese national bulletins ABCE (1985–1997), provincial bulletins by the Yunnan Seismological Bureau and the Sichuan Seismological Bureau (1980–1997), and the ISC bulletins

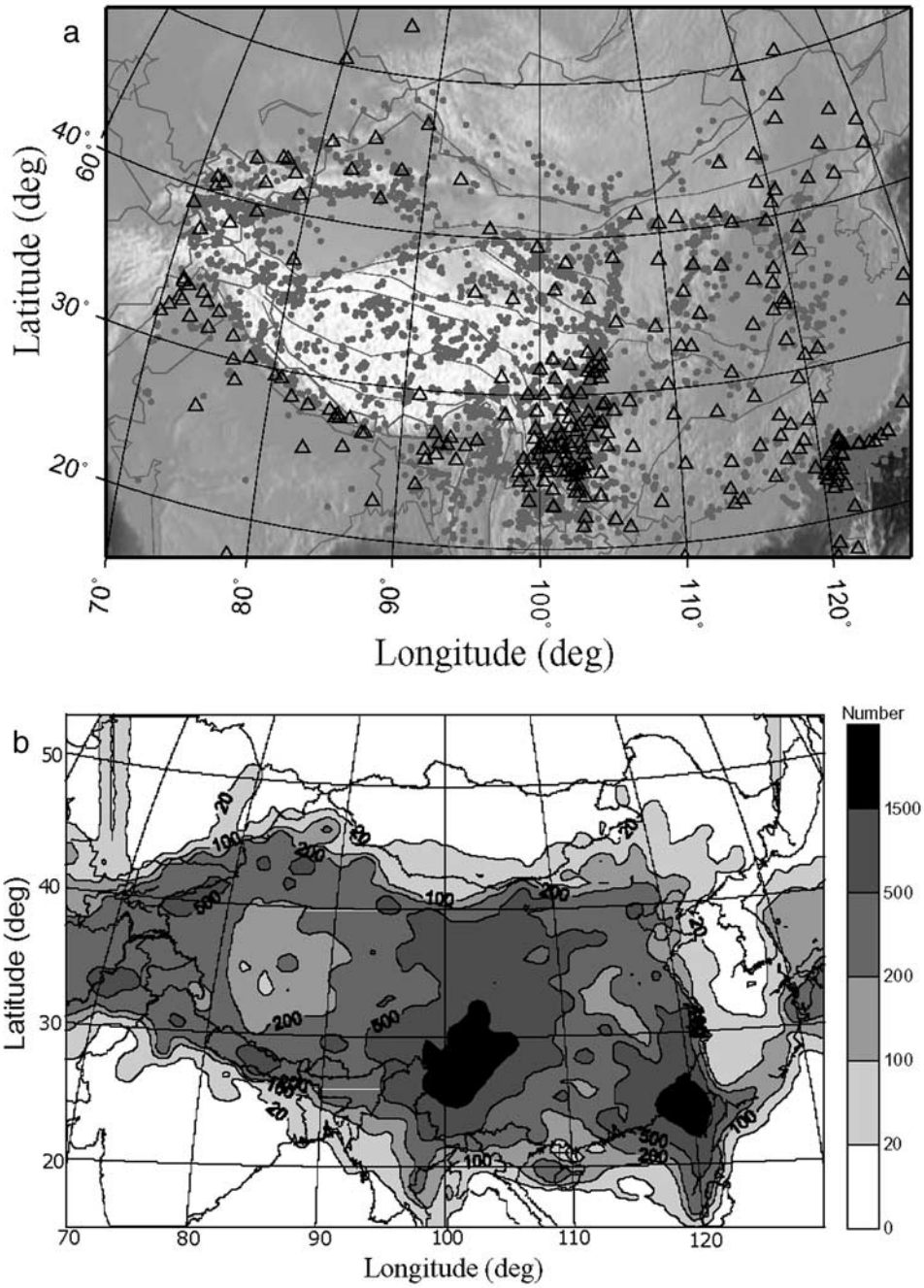

Figure 3. (a) Distribution of earthquakes (dots) and stations (triangles) and (b) the ray coverage used in this study. Plotted is the number of rays in each cell.

(1964–1997). Because of the large number of stations used and the diffusive nature of the seismicity in the Chinese continent and the neighboring region, we can achieve very dense ray coverage of the study area (Figure 3), even after imposing strict controls on data quality.

[18] The following criteria are used to select the data.

[19] 1. The epicentral distance Δ ranges from 2° to 12°. For a very thick crust of 70 km, the *Pn* starts to appear at 1.6°; it appears at smaller distances for a thinner crust. We also use arrivals that are labeled as *P* but continue to form a linear trend in the travel time curve up to distances of 12°.

[20] 2. The earthquake depth is limited to be less than 30 km and 40 km east and west of 107°E, respectively, to exclude limited number of earthquakes that may be in the mantle, e. g. under Tibet [*Chen and Molnar*, 1983; *Zhu et al.*, 1997].

[21] 3. The apparent velocity of rays is limited to be between 7.0 and 9.0 km/s [*Zhao and Xie*, 1993].

[22] 4. Every station has at least 10 *Pn* records to ensure more robust constraint on the station delays and every earthquake has at least 5 *Pn* records.

[23] 5. We use a method described in Appendix A to mitigate the problem of uneven data distribution. The

method aims to locate earthquake clusters and then choose the event with the highest number of observations in a cluster and discard all the other events in the same cluster. This procedure dramatically reduces the unevenness in the data distribution but still keeps the overall ray coverage of the study region intact.

[24] 6. After applying the above selection criteria, we use an iterative linear regression algorithm to derive our initial model for the average *Pn* velocity and average crustal thickness. The data with travel time residuals (relative to the initial model) larger than 6.0 s are discarded.

3.1. Initial Model

[25] The formula (5) and (6) below are used to calculate the initial model parameters: the average crustal thickness $\overline{H}$ and the average uppermost mantle *Pn* velocity $\overline{V}_m$. We choose the average crustal velocity ($\overline{V}_c$) of 6.3 km/s based on the study of *Li and Mooney* [1998] for our reference model.

$$\overline{H} = t_0 \Big/ \left(2\sqrt{1/\overline{V}_c^2 - 1/\overline{V}_m^2}\right) \tag{5}$$

$$\overline{V}_m = 1/\text{slope} \tag{6}$$

where t_0 and slope are the intercept time and the slope of the linear regression of travel time as a function of distance, respectively. All the travel times are corrected to the surface focus at the corresponding distances for the regression.

[26] Following our data selection procedures described above, we finally obtain 57,740 rays from 307 stations and 5433 earthquakes. We obtain the best fitting initial model with *Pn* velocity of 8.0 km/s and crustal thickness of 43.8 km. All the selected stations and earthquakes are shown in Figure 3a, and the data coverage is shown in Figure 3b.

3.2. Resolution

[27] To examine our model resolution, we perform two tests: (1) a conventional checkerboard test and (2) a test on an input model that resembles the anomalous regions of the actual inversion. In each test, synthetic data are generated using the real rays, which are then inverted using the same inversion procedure and parameters as in the actual inversion.

[28] Checkerboard tests are widely used although the method has intrinsic limitations [*Leveque et al.*, 1993]. For *Pn* velocity tests, our velocity perturbation is a sinusoidal pattern of 0.3 km/s in amplitude with respect to a background velocity of 8.0 km/s. For anisotropy tests, input anisotropy is a sinusoidal pattern of 3% in amplitude and the fast direction alternating at N-S and E-W directions. Several synthetic models with different wavelengths are tested. Results show we can resolve a pattern of 3° in half wavelength very well in almost all the study area for *Pn* velocity (Figure 4a) and for *Pn* anisotropy (Figure 4b). The resolution in bordering areas becomes poor. Note that the resolution depends both on the spatial and the azimuthal coverage of seismic rays, e.g., even though we have excellent ray coverage across the Taiwan Strait (Figure 3b), the resolution is still poor. The reason is that the rays in this region have similar azimuths (from earthquakes in Taiwan to stations in the mainland coasts).

[29] The resolution is quantified in a resolution map (Figure 5) using the resolvability as defined by *Zelt* [1998]. The resolvability, R, from a checkerboard test is defined as

$$R = \frac{\sum_{i=1}^{M} (t_i + r_i)^2}{2\sum (t_i^2 + r_i^2)},$$

where t_i and r_i are the true and recovered velocity anomalies at cell i inside a given area of M cells. We choose an operating area of 4.5° × 4.5° centered on the cell for which we want to calculate the resolvability. For the 0.5° cell spacing, M = 81. We use resolvability above 0.7 as an indication of a well-recovered checkerboard structure. The best resolved areas (with resolution of 2° × 2°) are the central part of the country, the north China area, and western Tarim and western Tibet.

[30] The second test we performed uses a synthesized input model that resembles the anomalous regions of the actual inversion (Figure 6, top). The areas with prominent fast and slow anomalies in the actual inversion are assigned a constant velocity perturbation of 0.3 km/s and −0.3 km/s, respectively. The cells with anisotropy amplitude larger than 1% in the actual inversion are assigned a constant anisotropy amplitude of 3% with the same anisotropy direction. All the other cells are assigned the background *Pn* velocity (8.0 km/s) with no anisotropy. Synthetic travel times of the real rays are calculated for this model and Gaussian noise is added to the synthetic data using a standard deviation that equals the root-mean-squares (RMS) of the residuals after the real inversion (1.33 s). Despite the large noise level added, the inversion recovers very well the structure of the velocity anomalies (Figure 6, bottom). The pattern of the anisotropy is also generally well recovered, but the anisotropy amplitude is significantly reduced after the inversion.

4. Inversion Results

[31] Our computation is done under flattened, layered Earth (equations (1)–(7)). However, our final values of *Pn* velocities and crustal thickness are given in the true spherical Earth, as by *Zhao and Xie* [1993] and *McNamara et al.* [1997]. To correct for sphericity, we use Earth-flattening transformation [e.g., *Aki and Richards*, 2002]. The actual crustal thickness $H = R_e(1 - e^{-H_f/R_e}) \approx H_f(1 - H_f/(2R_e))$, where H_f is the crustal thickness in the flattened Earth and R_e is the radius of the Earth, i.e., H is smaller than H_f by about a fraction of $H_f/(2R_e)$. The actual *Pn* velocity is the *Pn* velocity in the flattened Earth times $(R_e - H)/R_e$. For our reference model with crustal thickness of 43.8 km and *Pn* velocity of 8.0 km/s, the crustal thickness and *Pn* velocity in the flattened Earth are 44.0 km and 8.06 km/s, respectively.

[32] Our inversion results are shown in Figure 7 for *Pn* velocity and anisotropy and in Figure 8 for station delays. The errors of these parameters are obtained by the bootstrap

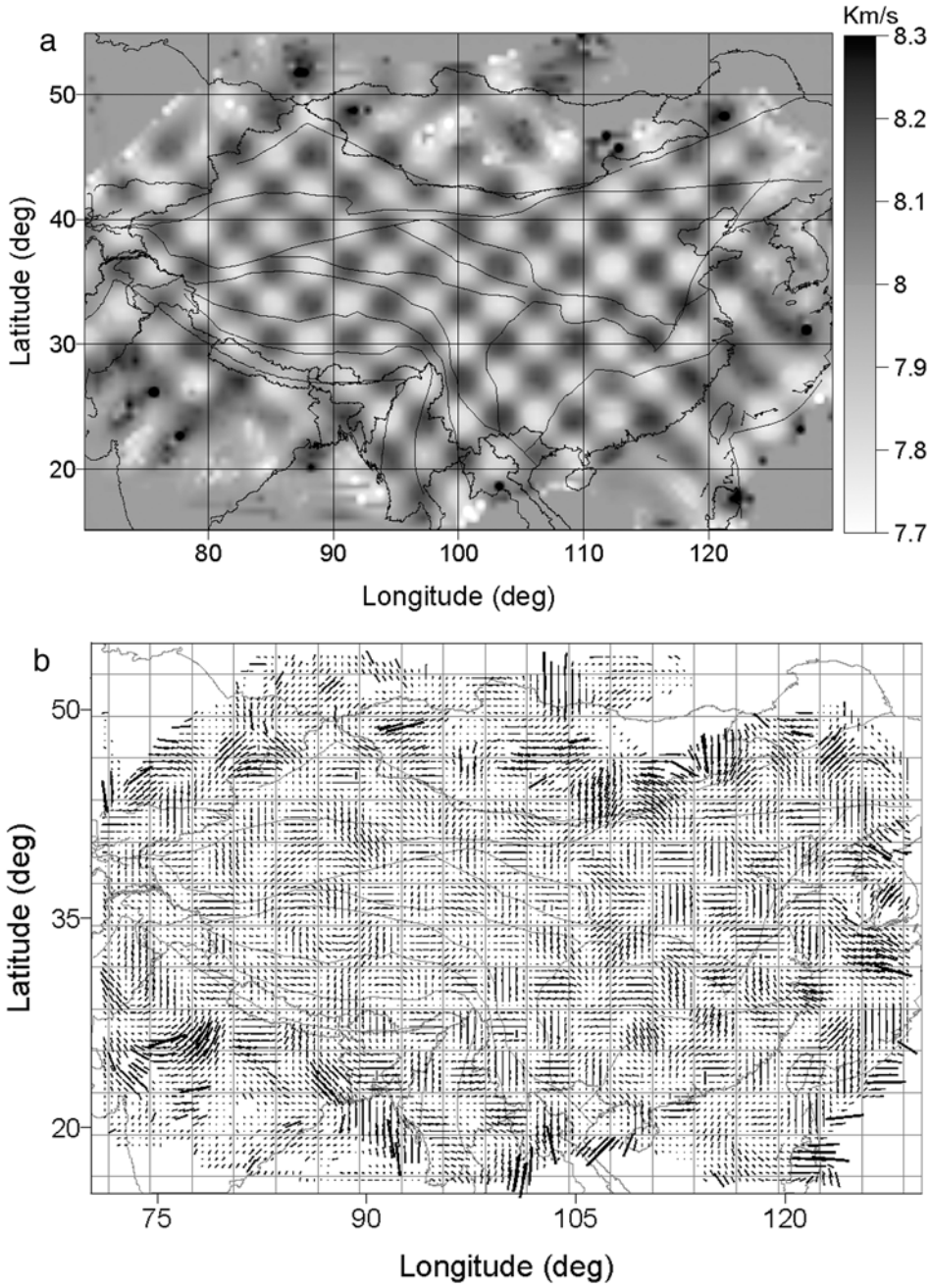

Figure 4. Checkerboard resolution tests on (a) *Pn* velocity and (b) *Pn* anisotropy. The input is a sinusoidal pattern of 3° in half wavelength. The input velocity has the amplitude ±0.3 km/s with respect to a background velocity of 8.0 km/s. The input anisotropy has amplitude of 3% and fast direction alternating at N-S and E-W directions in the neighboring cells.

method [e.g., *Tichelaar and Ruff*, 1989]. The errors in the *Pn* velocities are almost all less than 0.05 km/s (Figure 9) (except for bordering areas). Figure 10 shows the ratio of the standard error and the anisotropy amplitude for areas with relatively large anisotropy (amplitude larger than 1.0%). The anisotropy amplitudes are almost all larger than 2–3 times the standard errors. The mean of the standard errors of the station delays is 0.28 ± 0.06 s (2σ). For station delays with amplitude larger than 0.3 s, 96% of them have amplitudes larger than the standard errors and 82% of them have amplitudes larger than two standard errors.

[33] Figure 11 shows travel time residual distribution before and after the inversion. The inversion reduces the RMS error of the residuals from 1.85 s to 1.33 s. The reasons for the relatively small variance reduction (48%) are not clear. Possible causes include (1) data errors, including errors in arrival times picks and misindentification of *Pn* phases; (2) errors in earthquake locations; (3) the trade-off between the smoothed solution and the misfit; and (4) small-scale variation in crustal velocity and thickness that cannot be accounted for by static station and earthquake delay terms.

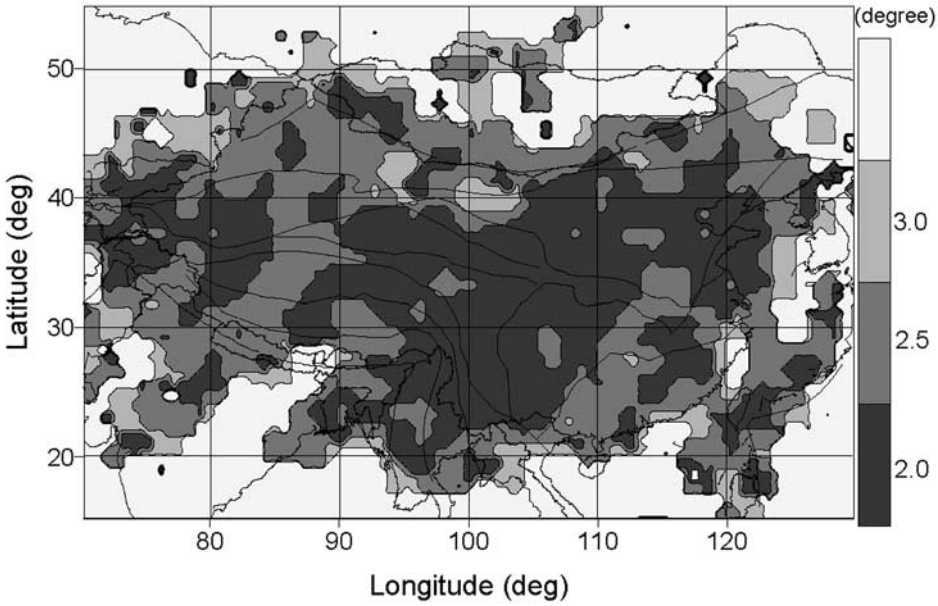

Figure 5. Resolution map for *Pn* velocities from checkerboard tests (see text). The resolution for most parts of China ranges from 2° × 2° to 3° × 3°.

[34] Below we describe the general features of our inversion first and discuss later a few areas of particular interest (north China, the Tibetan Plateau, and Sichuan-Yunnan region) in section 5.

4.1. *Pn* Velocity Variation

[35] The *Pn* velocity ranges from less than 7.7 to over 8.3 km/s. Generally, the *Pn* velocity in western China is higher than in eastern China. Our inversion reveals significant features that correlate with surface geology. Perhaps the overall most striking feature of the *Pn* velocity is a mosaic of very fast and very slow anomalies across the region, which provides a mirror image of the heterogeneous geology of China as we briefly summarized in the introduction.

[36] Prominent high *Pn* velocities (8.1–8.3 km/s) are found in four major basins bordering the Tibetan and/or Tien Shan (western Tarim, Junggar, Tulufan, Qaidam, and Sichuan basins). These basins are tectonically stable with weak deformation, lack of seismic, thermal, and volcanic activities. Thus the high *Pn* velocity anomaly is likely the signature that these basins are strong and cold. Note also, not all of the Tarim basin has fast *Pn*: the values (8.0–8.1 km/s) for the eastern Tarim is only about or slightly above the average.

[37] Prominent low *Pn* velocities are observed in several localities: beneath the northern Tibetan Plateau, Tien Shan, the southern part of south China (including northern Hainan), and north China. *Pn* velocity changes from high (8.0–8.2 km/s) in southern Tibet to very low (7.8–8.0 km/s) in northern Tibet. The low *Pn* velocity in the north correlates with Quaternary volcanism found in the region [*Deng*, 1978; *Arnaud et al.*, 1992; *Turner et al.*, 1993]. The result is consistent with previous *Pn* studies of the Tibetan Plateau [*Zhao and Xie*, 1993; *McNamara et al.*, 1997]. However, the *Pn* variation in our model is more complex. The low-velocity anomalies can be traced all the way across southwestern Tibet and south central Tibet to near the India plate along 82° and 90° longitudes, respectively.

[38] A large area of pronounced low *Pn* velocity is found beneath the NCB with Precambrian basement. This is in sharp contrast to high velocity generally found beneath old cratons and stable blocks, such as the Canadian Shield and the four major basins in west China. Pronounced low *Pn* velocity is also observed in south China, beneath much of the Guangxi Autonomous region and the Guangdong province down to northern Hainan. This is consistent with a Hainan plume beneath the hot spot-type volcanism in the region proposed by *Lebedev and Nolet* [2003]. They observed slow *S* anomaly beneath the same region from the surface down to depths of at least 660 km. The western Tien Shan (west of the Chinese border) shows pronounced low *Pn* velocity (about 7.8–7.9 km/s), but the eastern Tien Shan (between Tarim and Junggar basins) shows relatively high velocity (about 8.1–8.2 km/s).

[39] A high-velocity anomaly and a low-velocity anomaly are found beneath Bangladesh and eastern India and beneath Myanmar, respectively. Active volcanoes of the region (Popa, Lower Chindwin, and Singu Plateau volcanoes in Myanmar, and Tengchong volcano in western Yunnan, China) are associated with low *Pn* velocity. The boundary of the fast and slow anomalies coincides nicely with the India-Eurasia collision zone along the mountain ranges bordering eastern India and Myanmar, suggesting the fast and slow anomalies may be due to strong India lithosphere and weak Eurasia lithosphere as well as the continent-continent collision.

[40] We also observed slow anomaly beneath the East China Sea margin, the Okinawa trough, and the Taiwan

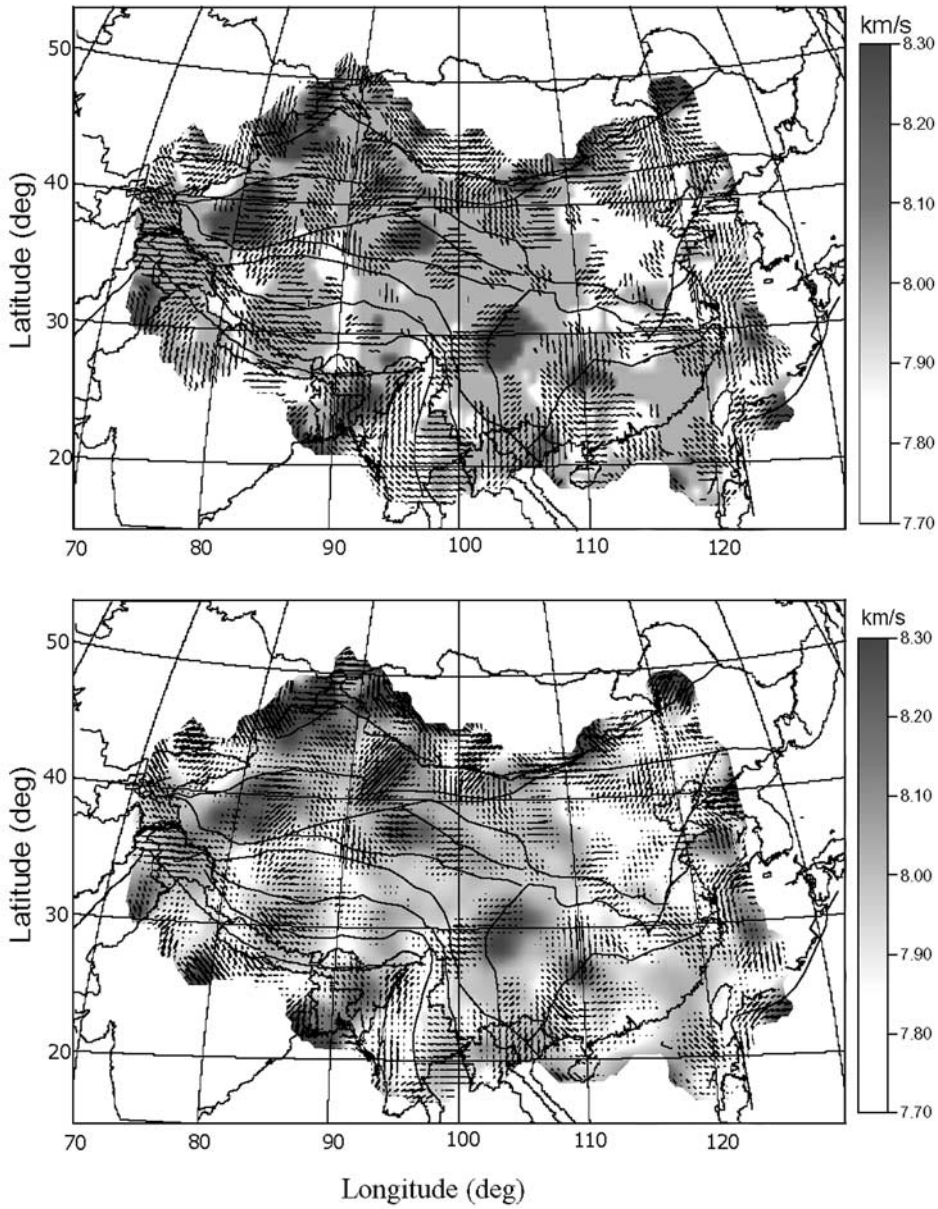

Figure 6. (bottom) Resolution test result for a synthesized input model that resembles the anomalous regions of (top) the actual inversion. The input velocity anomalies have a constant perturbation of 0.3 km/s or −0.3 km/s with respect to the background velocity of 8.0 km/s. The input anisotropy, where specified, has a constant amplitude of 3%. Gaussian noise with a standard deviation of 1.33 s is added to the synthetic travel times before inversion.

island and fast anomaly beneath Ryukyu trench, which may be related to the subduction of the Philippine plate beneath Eurasia.

4.2. *Pn* Anisotropy

[41] The dominant source of anisotropy in continental upper mantle is likely from the lattice-preferred orientation (LPO) of olivine through deformation [*Nicolas and Christensen*, 1987]. Natural samples of peridotites suggest that olivine *a* axis (fast direction) is within the foliation plane parallel to the lineation direction [*Silver*, 1996]. Deformation tends to align the *a* axis in the direction of major strain axis [*Ribe*, 1992]. Thus, if the crust and subcontinental mantle deform coherently, the so-called vertically coherent deformation (VCD) model by *Silver* [1996], then the mantle anisotropy would reflect the last significant deformation environment, e.g., parallel to the direction of maximum shearing under simple shear regime, or perpendicular to the direction of maximum compression under collisional regime, or parallel to the direction of extension under extension or rifting regime.

[42] Figure 7 shows *Pn* anisotropy with magnitude larger than 1%. There appear some correlations between anisotropy and tectonic activities. Anisotropy in the anomalously fast regions of major basins (Sichuan, Tarim, and

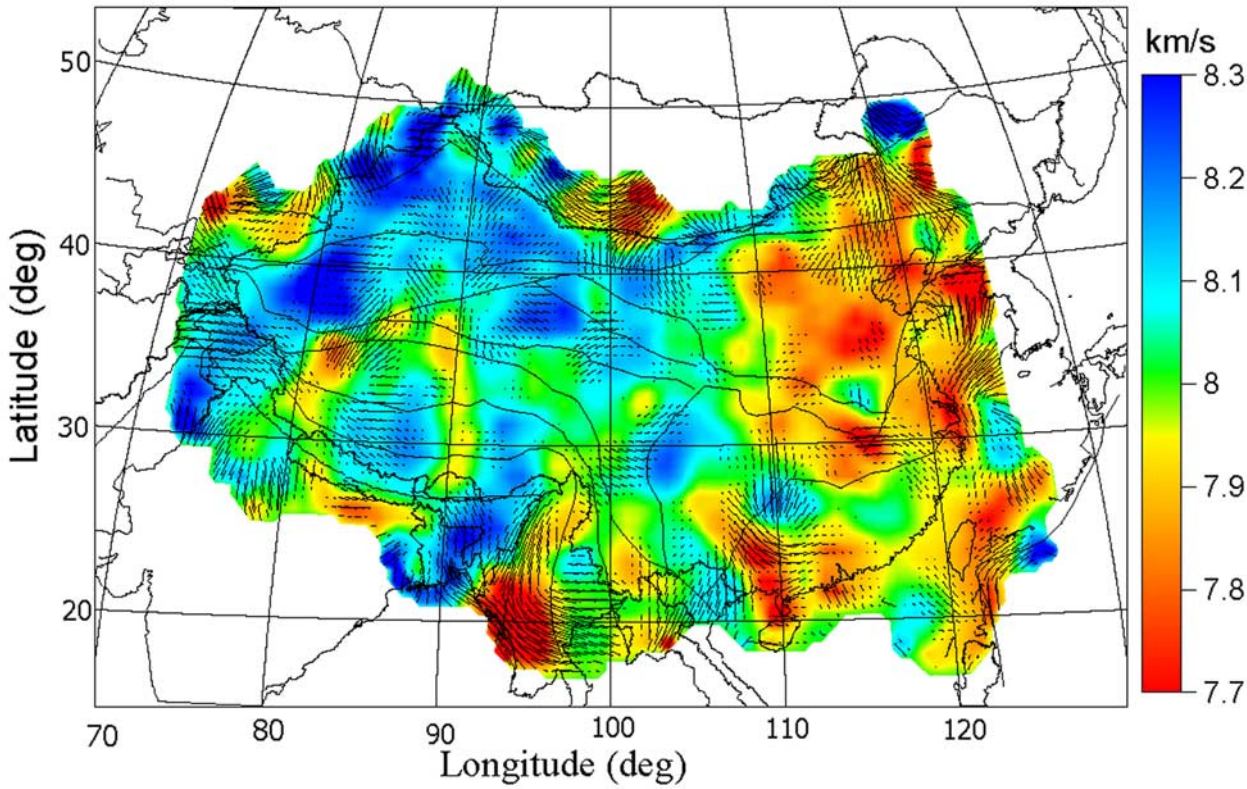

Figure 7. Inversion results for *Pn* velocity (color) and anisotropy (bars). Red and blue indicate saturated for low velocity at 7.7 km/s and for high velocity at 8.3 km/s, respectively. The bar indicates the fast *Pn* direction, and the length is proportional to the anisotropy amplitude, saturated at 4%. Only anisotropies larger than 1% are plotted. Also plotted are major block boundaries (Figure 1) as well as country borders and coastlines.

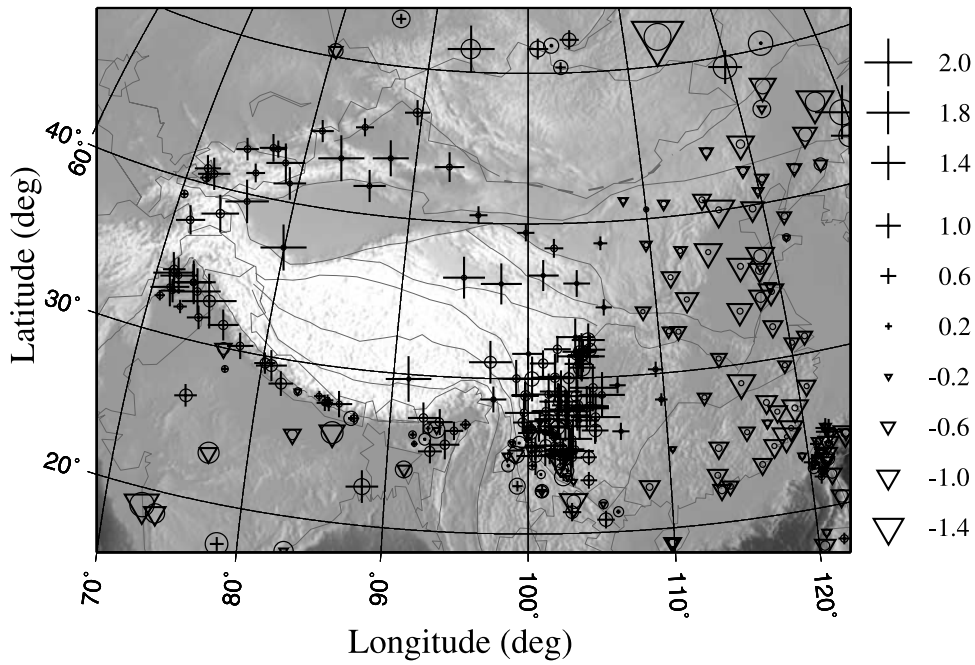

Figure 8. Station delays obtained in this study. Negative delays (triangles) is indicative of a thinner crust (thinner than the average 43.8 km of the reference model); positive delays (crosses) is indicative of a thicker than average crust. Circle indicates the standard error of the corresponding station delay.

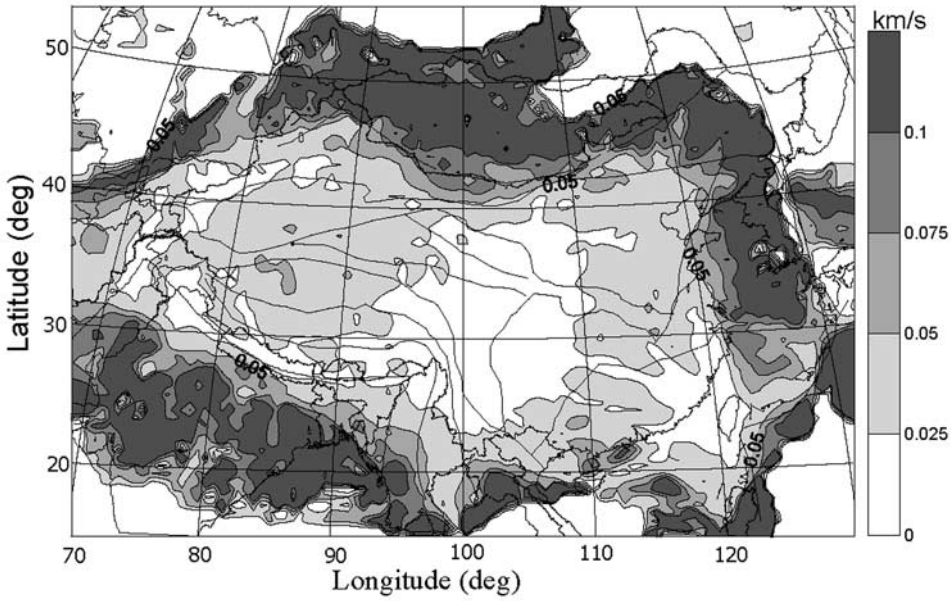

Figure 9. Standard errors of the *Pn* velocities obtained in this study. Almost all are less than 0.05 km/s (except for bordering areas).

Junggar) tends to be small, suggesting little deformation in these stable regions. High values of anisotropy are generally beneath high-deformation regions, including the Tibetan Plateau, western Tien Shan, western Sichuan and Yunnan and Myanmar, and part of north China, suggesting the anisotropy is likely related to present-day mantle deformation. An exception is the region in south central China east of Sichuan Basin and in Guangxi and Guangdong, which is relatively stable with low seismicity, but has strong anisotropy.

4.3. Station Delays and Crustal Thickness

[43] The station delays can be caused by crustal velocity (V_c) and crustal thickness (H) variations, relative to the reference model ($\overline{V}_c$, $\overline{H}$). The station delay is

$$H\eta - \overline{H}\overline{\eta} = H\sqrt{1/V_c^2 - 1/\overline{V}_m^2} - \overline{H}\sqrt{1/\overline{V}_c^2 - 1/\overline{V}_m^2}, \qquad (7)$$

where $\eta = (1/V_c^2 - 1/V_m^2)^{1/2}$ is vertical slowness in the crust. In most parts of China, the average crust velocities yielded

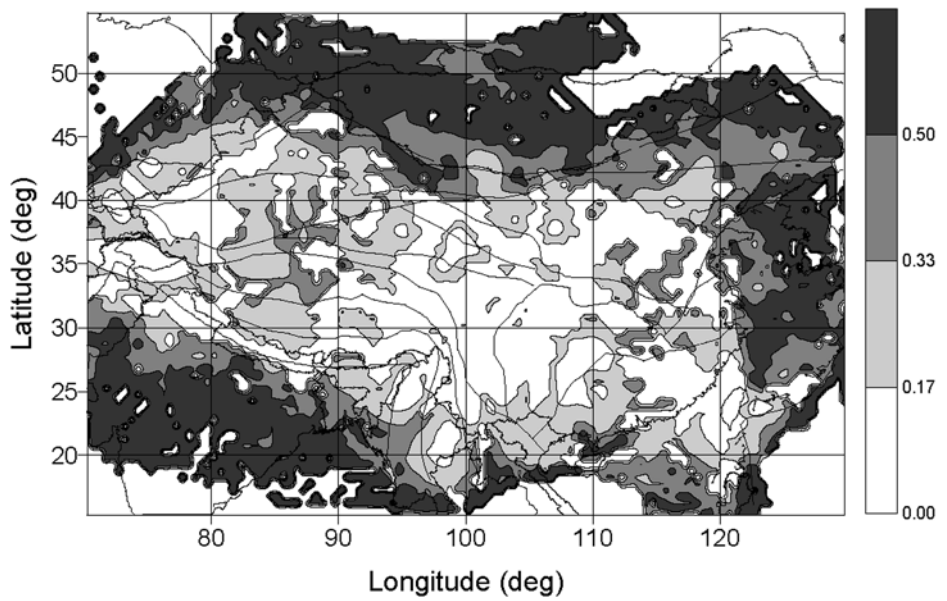

Figure 10. Ratio of the standard error and the anisotropy amplitude for areas with relatively large anisotropy (amplitude larger than 1.0%). The amplitudes are almost all larger than 2–3 times the standard errors (except for bordering areas).

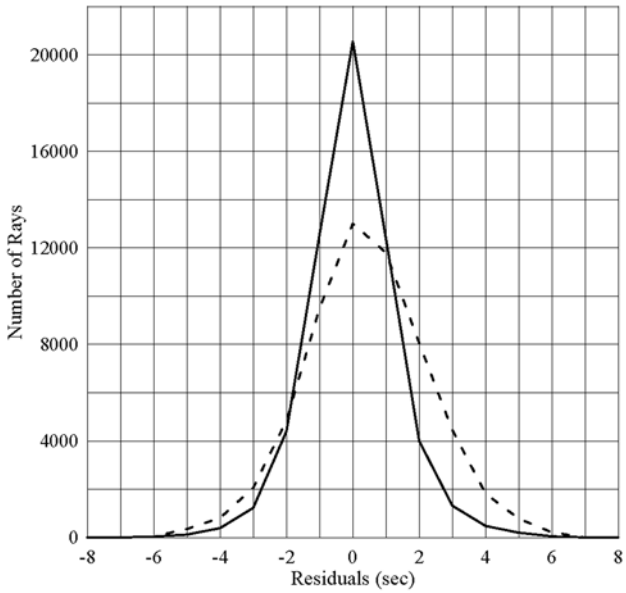

Figure 11. Distributions of the travel time residuals before and after the inversion.

from 36,000 km deep seismic sounding (DSS) range from 6.15 to 6.45 km/s [*Li and Mooney*, 1998]. Their average velocity for China is about 6.3 km/s. From equation (7), a 0.2 km/s variation in crustal velocity results in about 0.36 s, (assuming $\overline{H}$ = 44 km and $\overline{V}_m$ = 8.0 km/s). Thus the observed station delays, ranging from −1.5 to 2.6 s, are mainly from the variation in crustal thickness. If we attribute all the station delays to variation in crustal thickness, one second delay corresponds to 10.2 km difference in crustal thickness from equation (7). Because earthquake depths are often poorly constrained, earthquake delays are strongly influenced by the uncertainty in earthquake depths. For this reason, we do not use the earthquake delay times to infer crustal thickness.

[44] Figure 12 shows crustal thickness contours based on the station delays (Figure 8), assuming the crustal velocities from the global crustal model CRUST 2.0, which is specified on a 2° × 2° cell [*Bassin et al.*, 2000]. The errors in the stations delays, 0.28 ± 0.06 (2σ), would result errors of crustal thickness estimates of about 2.2–3.5 km. If the actual crustal velocity differs by 0.2 km/s from CRUST 2.0, the estimated crustal thickness would have errors of 3 km and 6 km for a 30 km and 70 km thick crust, respectively. Despite these uncertainties, our estimates of crustal thickness from the station delays give an independent, first-order estimate of the crustal thickness variation in China. Because station delays are affected by crustal thickness immediately beneath the stations, they also provide new data coverage for estimating crustal thickness where, for example, DSS profiles are not available. Note also the contours are likely to have large errors in the areas where there are few stations, such as the Tibetan Plateau and all the major basins in the west (Sichuan, Qaidam, Tarim, Junggar, and Tulufan basins). These contours are controlled by stations at the rims of the blocks. Some general features of station delays and crustal thickness are as follows:

[45] 1. With the exception of two stations in the edges of our map (one in Siberia and one in India) (Figure 8), the station delays range from −1.5 to 2.6 s, which correspond to crustal thickness of about 29 to 70 km. The delays in the eastern China are almost all negative, indicating a crust thinner than the average (43.8 km). On the other hand, the delays of the stations in the west are almost all positive, indicating a crust thicker than 43.8 km. Compared with the topography of China, it is clear the difference in crustal

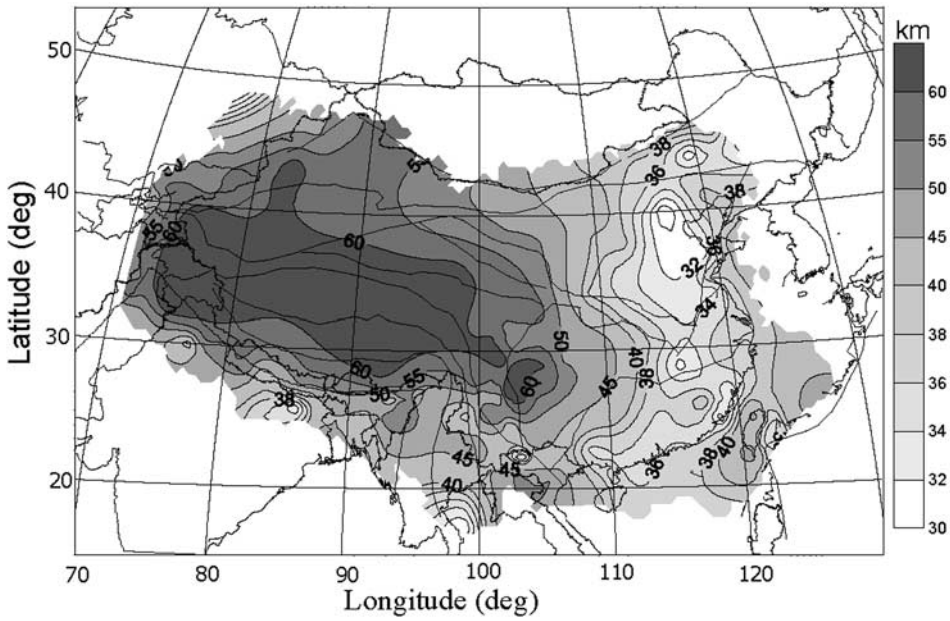

Figure 12. Crustal thickness contours based on the interpretation of the station delays assuming crustal velocity from CRUST 2.0 [*Bassin et al.*, 2000]. Note that in the regions with few stations (central Tibetan Plateau, the major basins in the west), the contours have large errors.

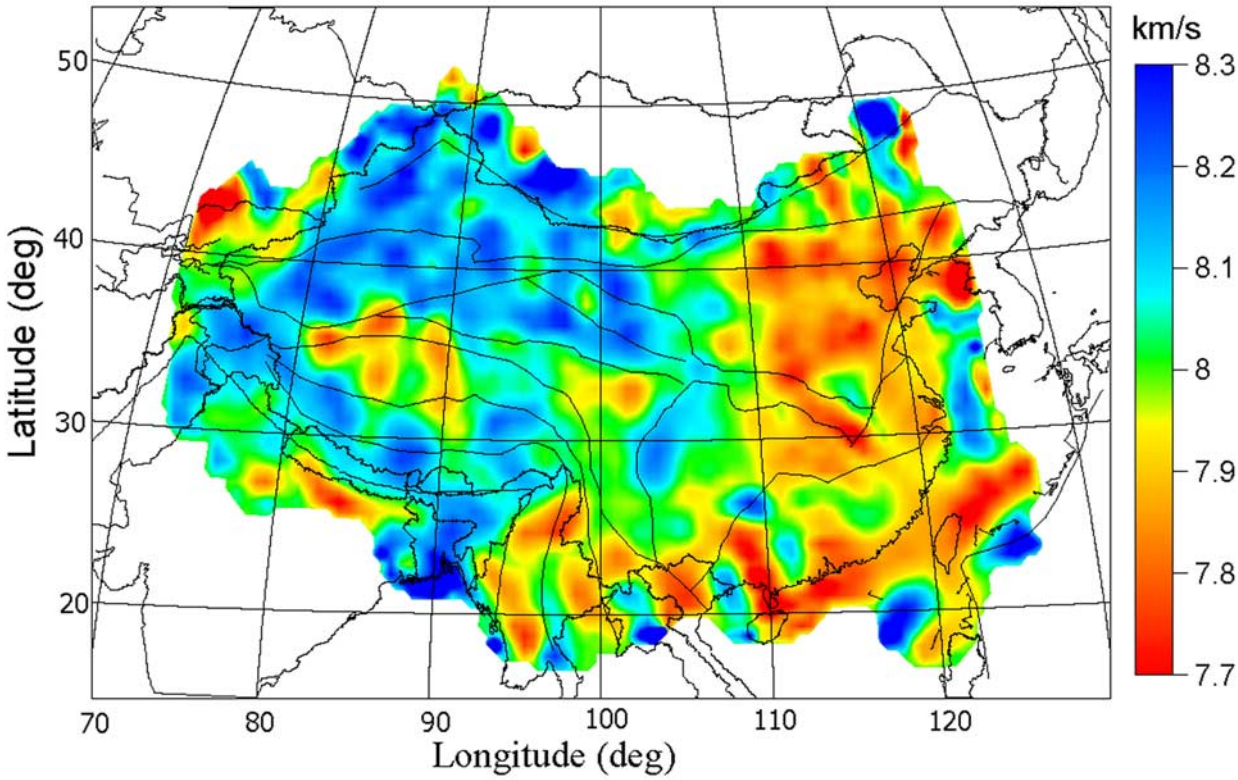

Figure 13. Results for *Pn* velocity (colors) from an inversion that does not include the *Pn* anisotropic terms. Color scale is the same as Figure 7.

thickness between the eastern and western parts of China is due to airy isostasy to the first order.

[46] 2. We observe a sharp change in station delays across the India-Himalaya collision. Almost all of stations on the Indian plate show negative or near zero delays but all the neighboring stations in the Himalayas show large positive delays. This suggests a very sharp change in crust thickness across the boundary (by 10–20 km over a small distance range).

[47] 3. The station delays in the Longitudinal Valley and the Coastal Range in eastern Taiwan are consistently negative while the station delays at the Coastal Plain and West Foothills are either positive or close to zero, suggesting thinner crust along the eastern coast of the island than along the western plain. Note that the resolution for Taiwan is not very good because of poor azimuthal coverage of the rays. Thus we believe the relative station delays are more robust than the absolute delays.

[48] 4. The station delays in the eastern margin of the Tibetan Plateau vary significantly, suggesting large variation in crustal thickness of the region.

5. Discussion

5.1. Inversion Without Anisotropy

[49] To compare with other *Pn* studies that did not include anisotropy and to examine the effect of including the anisotropy in our inversion, we also conducted an inversion that does not include the anisotropic terms in equation (1) but otherwise follows the same inversion procedure with the same parameters. The inversion results (Figure 13) are generally consistent with those of the inversion with anisotropy (Figure 7). The velocity anomaly patterns are almost exactly the same in the eastern half of the country (east of 100°E), where the ray coverage is considerably better (Figure 3b).

[50] However, there are some differences in the western half of the country. The fast anomalies near the major basins in the northwest (Tarim, Junggar, Tulufan, and Qaidam) in Figure 13 (inversion without anisotropy) are more scattered in the inversion without anisotropy, while the fast anomalies in Figure 7 (inversion with anisotropy) delineate the location of the basins better. Another important difference is in the Tibetan Plateau. The slow anomalies in Figure 13 are mostly concentrated in the northern Tibet, while the slow anomalies in Figure 7 extend to near the Indian Plate along the longitudes of 82°E and 90°E, respectively. Although our ray coverage in central Tibet is the poorest, our resolution test suggests we can resolve this more complex structure (Figure 6). The results suggest possible trade-off between the velocity anomalies and anisotropy when ray coverage is not sufficient. Thus it is important that the model of the Tibet be further tested with increasing spatial and azimuthal ray coverages.

5.2. Comparison With Previous Studies

[51] Inversions of *Pn* travel times in China have recently been conducted by *Wang et al.* [2002] and *Sun et al.* [2004]. Both studies used a subset of the data we used here. The data used by *Wang et al.* [2002] and *Sun et al.* [2004] are

Table 1. Crustal Thickness at Selected Regions

Regions	This Study	*Li and Mooney* [1998]	*Sun et al.* [2004]	Zhu[a]
North China	30–40	30–40	30–40	30–40
East China	32–40	30–33	30–35	32–40
N-S Belt	40–60	40–60	40–60	40–60

[a]J. S. Zhu (personal communication, 2003), based mostly on DSS profiling.

arrival times from the ABCE (1986–1996) and the ABCE (1990–1998), respectively. The inversion procedure used by *Wang et al.* [2002], which also includes *Pn* anisotropy, is very similar to the one used here; both follow the same basic scheme of *Hearn* [1996]. *Sun et al.* [2004] obtained a 3-D *P* velocity model of China using a new tomography method which pieces together individually derived 1-D models (no anisotropy is considered). Their results include maps of *Pn* velocity and crustal thickness.

[52] Our results show good agreement with the results of these two studies on large-scale structures. The model of *Wang et al.* [2002] shows prominent fast anomalies in Sichuan, Qaidam, Tarim, and Junggar basins as in our model. Their model also show the broad slow anomaly in north China and the slow anomaly in Guangxi-Guangdong-Hainan. The patterns of the *Pn* anisotropy are also generally consistent with our model. The model of *Sun et al.* [2004] shows clear fast *Pn* anomalies in Sichuan and Tarim basins, slow anomaly in north China, and relatively slow anomaly in the northern Tibet. It also shows some evidence for fast anomaly in Junggar and slow anomaly in Guangdong.

[53] However, our model shows considerably better resolution, particularly in the regions of Tibet, the eastern Himalayan syntaxis, and north China. In addition, *Sun et al.* [2004] show a large area of fast anomalies in the eastern and southern Tibet, which is not evident in our and *Wang et al.*'s [2002] models.

[54] Our inferred crustal thickness is generally consistent with previous studies (Table 1). The values for north China are very similar. All models show that the crust thickens rapidly increase across the "N-S belt" of large topography change and active seismicity (around 110–100°E) from about 40 km in the east to about 60 km in the west and that the crust in the Tibetan Plateau thickens toward the central part of the plateau. However, our crustal thickness in eastern China is significantly thicker than those of *Li and Mooney* [1998] and *Sun et al.* [2004], but is compatible with a recent crustal thickness map by J. S. Zhu (Chengdu University of Technology, personal communication, 2003), which is based mostly on a large compilation of DSS profiling data. The models of *Li and Mooney* [1998] and *Sun et al.* [2004] indicate that the crust of the entire eastern and southeastern China has nearly uniform thickness (ranging from 30 km to 33 or 35 km). It is unclear to us whether the discrepancy is due to resolution or inconsistency of different data sets.

5.3. North China

[55] A large area of northern China is underlain by the Sino-Korean (north China) Craton basement, consisting of Archean and Proterozoic metamorphic and igneous rocks [*Zhang et al.*, 1984; *Griffin et al.*, 1998]. Much of the craton remained stable up to about Triassic times, with well-developed sedimentary strata. However, since the late Mesozoic, the region has been tectonically active, with the development of large rifted sedimentary basins and widespread volcanism [e.g., *Gilder et al.*, 1991; *Li et al.*, 1995; *Menzies and Xu*, 1998; *Ren et al.*, 2002]. The region has high heat flow of up to 100 mW/m^2 [e.g., *Ma et al.*, 1984; *Liu*, 1987] with the average of about 80 mW/m^2 in the north China-Bohai basin area. The region is one of the most active areas of intracontinental earthquakes in the world. Four major ($M > 7$) destructive earthquakes (Xingtai, Bohai, Haicheng, and Tangshan) occurred during the last major burst of seismicity in a decade between 1966 and 1976 [*Ma et al.*, 1990].

[56] North China stands out in our model. A large area of north China shows prominent low *Pn* velocity and the crust there is the thinnest of the whole study area. A direct linear fitting of the *Pn* data that sample the area of longitudes 110–122°E and latitudes 27–42°N yields the average velocity of 7.86 km/s and the average crust thickness of less than 36.6 km. The thinnest crust is located in the north China basin (Figure 12). The elongated shape of the crustal thickness contours, trending NNE, correlates well with the shape of the NNE trending north China basin and the Songliao basin, with the crust thickening beneath the Daxin'anling and Taihang mountain ranges to the west. The boundary along the Daxin'anling and Taihang mountain ranges between the thicker crust to the west and thinner one to the east roughly follows the major lineament of the Bouguer gravity anomaly [e.g., *Teng et al.*, 1983; *Griffin et al.*, 1998].

[57] The causes for these anomalous observations and the dynamics of the region are poorly understood. Most observations (basin development, volcanism, high heat flow, low mantle velocity, thin crust) are consistent with the notion that the region has been under extension and rifting since Late Mesozoic [*Ren et al.*, 2002]. Furthermore, the high heat flow, Cenozoic volcanism, and low *Pn* velocity may suggest hot mantle upwelling. Geophysical data seem to suggest a thin lithosphere at present (50–120 km) beneath the basins [*Liu*, 1987]. However, mantle xenoliths suggest the craton was underlain by an Archean lithospheric keel of 200 km thick [e.g., *Griffin et al.*, 1998], which was replaced by a new lithosphere after the Paleozoic [*Gao et al.*, 2002]. Thus perhaps the mantle lithosphere may have been thinned by as much as 80–150 km during the rifting period in the Late Mesozoic and Cenozoic, by extensional stretching and by convective removal from mantle upwelling.

[58] Quantitative models of rifting and mantle upwelling in north China (and the larger East Asia margin area) are lacking. Speculation on the mechanisms [e.g., *Liu*, 1987; *Barry and Kent*, 1998; *Griffin et al.*, 1998; *Ren et al.*, 2002] often invokes the extension from a far-field effect of the India-Eurasia collision and the back-arc extension and mantle upwelling related to the subduction of the Pacific plate beneath the Eurasia. Extension along the East Asia margin was interpreted as a pull-apart effect due to the eastward ejection of crustal blocks from the India-Eurasia collision zone [*Molnar and Tapponnier*, 1975; *Tapponnier et al.*, 1982]. However, *Northrup et al.* [1995] suggested that the extension may be related to the decrease in convergence rate between the Pacific and Eurasia plates from the Paleocene through middle Miocene.

[59] One significant observation that must be addressed by a realistic model is that the primary strain in north China at present, at least at the midcrust and lower crust, is not that of pure extension but a dextral simple shear in the NNE direction based on the fault slips of major earthquakes [*Chen and Nabelek*, 1988]. *Chen and Nabelek* [1988] proposed that the north China basin has developed as a composite pull-apart basin due to right-lateral slip on strike-slip fault systems since the Eocene. *Zeng et al.* [1995a] suggested that the shallow crust (to 6–8 km) is dominated by extension and normal faulting, but the deeper crust is dominated by strike-slip faults. The change of stress regimes with depth may be explained by magmatic intrusion from the upper mantle to the midcrust.

[60] Our result on *Pn* anisotropy in northern China is quite complex. No significant anisotropy is observed beneath the southern part of north China and beneath Bohaiwan with very low *Pn* velocity. However, strong *Pn* anisotropy is observed beneath northern Taihang mountain, Yan mountain, and southern Daxin'anling mountain. The fast direction is roughly NNE to N-S, which seems consistent with a dextral simple shear in the NNE direction in the mantle lithosphere. This result is similar to the Basin and Range in the western United States, where mantle anisotropy does not agree with extension direction at surface (i.e., the VCD model of deformation [*Silver*, 1996] does not apply in these extensional basins).

5.4. Tibetan Plateau

[61] Our data coverage in Tibet is much denser than those of previous studies [*Zhao and Xie*, 1993; *McNamara et al.*, 1997]. The number of *Pn* rays we used is 28,451 for an area (70–110°E, 25–45°N) smaller than that of *McNamara et al.* [1997], which is an increase of at least 19 times. Excluding the dense ray coverage at the eastern margin, our number of rays is 11866 in the area (70–100°E, 25–45°N). The coverage is still poor compared with the data coverage in other areas of this study (Figure 3b). Note in particular the lack of stations inside the Tibetan Plateau and the Tarim basin. Caution is required when interpreting the crustal thickness contours in those blocks.

[62] Low upper mantle velocities in both *P* and *S* waves in northern Tibet and fast shield-like upper mantle velocities in southern Tibet were well documented [*Chen and Molnar*, 1981; *Lyon-Caen*, 1986; *Brandon and Romanowicz*, 1986; *Zhang and Lay*, 1996; *Holt and Wallace*, 1990; *Zeng et al.*, 1995b; *Rodgers and Schwartz*, 1998]. Propagation of *Sn* was found inefficient in northern Tibet and very efficient in southern Tibet [*Barazangi and Ni*, 1982; *McNamara et al.*, 1995; *Rapine et al.*, 1997]. These observations were used to suggest underthrusting of cold Indian continental lithosphere beneath southern Tibet [e.g., *Ni and Barazangi*, 1983; *Beghoul et al.*, 1993]. The low mantle velocities and abundance of Quaternary volcanism in northern Tibet are consistent with melting of mantle lithosphere from convective removal of mantle lithosphere [*Houseman et al.*, 1981; *Molnar et al.*, 1993].

[63] Our models generally agree with *Pn* velocity inversions of the Tibetan Plateau of *Zhao and Xie* [1993] and *McNamara et al.* [1997] (which did not include anisotropy). The agreement is remarkable between our inversion without anisotropy (Figure 13) and that of *McNamara et al.* [1997]. However, our models present a much sharper image and finer scale structure, e.g., of the low anomaly in the Qiangtang block. The difference is likely due to our much increased ray density, which allows us to resolve smaller-scale structure. Our inversion with *Pn* anisotropy included (Figure 7) shows a more complex finer scale structure of *Pn* velocity variation in southern Tibet. The low-velocity anomalies can be traced from northern Tibet across southwestern Tibet and south central Tibet to near the India plate along 82°E and 90°E longitudes, respectively. In light of significant mantle anisotropy present in this region from this study and shear wave splitting data, it is important to keep in mind the potential biases from the trade-off between the velocity anomalies and anisotropy when ray coverage is not sufficient. Our observation of the complex structure in the southern Tibet cannot be explained by existing 2-D models of the Tibetan Plateau and suggests that the lithospheric dynamics under Tibet must be 3-D [*Molnar et al.*, 1993; *Dricker and Roecker*, 2002].

[64] The pattern of the *Pn* anisotropy in the Tibetan Plateau is complex. Limited observations of *SKS* splitting were made previously. For horizontal lineation of LPO olivine (*a* axis), both the fast *Pn* direction and the fast polarization of near-vertically traveling shear waves are parallel to lineation direction. *Pn* anisotropy is absent beneath much of the Himalaya block, which agrees with *SKS* splitting data [*Sandvol et al.*, 1997; *Chen and Ozalaybey*, 1998]. Consistent anisotropy is present beneath the Lhasa block. The fast direction is predominately E-W, parallel to the collision boundary (perpendicular to the direction of maximum compression). This is also consistent with *SKS* splitting data [*Silver*, 1996]. Large anisotropy (up to 4%) is observed beneath parts of northern and western Tibet with low *Pn* velocity and the fast direction is nearly NNE to N-S directions. The fast direction departs from the *SKS* splitting fast direction, which is E-W to ENE, along the Yadong-Golmud Geotransect (between 90°E and 94°E), which is the only profile where a large number of shear wave splitting measurements are available [*McNamara et al.*, 1994; *Silver*, 1996; *Chen and Ozalaybey*, 1998]. Because *SKS* splitting is accumulated along the whole path in the mantle beneath the station, the difference between the *Pn* fast direction and that of the shear wave may represent a change of mantle (olivine) crystal alignment along the depth of the mantle lithosphere and the asthenosphere. The change of the *Pn* anisotropy in our model at about 30°N and again at about 33°N agrees well with the changes in *SKS* splitting and Bouguer gravity anomalies along the Yadong-Golmud profile, observed by *Chen and Ozalaybey* [1998]. They interpreted the changes by the juxtaposition of Indian lithosphere against the overlying Eurasian lithosphere in which the Eurasian lithosphere terminates at 30°N and the Indian lithospheric mantle extends to 33°N. The change in *Pn* anisotropy between northern Tibet and southern Tibet (Lhasa and Himalaya blocks) suggests that the dynamic regimes of the two regions may be fundamentally different.

5.5. Sichuan Basin and the Interaction Between the Tibetan Plateau and Yangtze Craton

[65] The pattern of station delays in the eastern margin of the Tibetan Plateau is very complex (Figure 8), suggesting significant crustal thickness variation in the region. Large

anisotropy is observed beneath western Yunnan and Myanmar, suggesting strong lithospheric deformation. We also find the surface location of the Sichuan basin is slightly shifted (by about 100–200 km) to the east relative to the high *Pn* velocity anomaly (Figure 7). The result is quite robust because of the dense ray coverage of the Sichuan-Yunan region (Figure 3b). At the surface, the east margin of the Tibetan Plateau is well developed with north-south striking faults. Mountain belts and rivers turn sharply from nearly west-east direction to the south and southeast direction. The latest GPS observations of the movement of east Asia clearly shows that the moving direction of materials of the region rapidly turns from the east direction to south and southeast [*Wang et al.*, 2001]. In the northwest margin of the Sichuan basin is the Longmen Shan thrust fault belt, which separates the Tibetan Plateau in the west and Yangtze craton in the east [*Korsch et al.*, 1997]. However, to the east, the Sichuan is much more stable, without any major faults or earthquakes. The *Pn* anisotropy of the basin area is also very small.

[66] A group of large magnitude of anisotropy orients nearly north-south in central China; to the east is the fault-bearing Yangtze platform and to west is the stable Sichuan basin (Figure 7). This region possibly marks the east boundary of the Sichuan basin. The positive station delays are very large in east of the Sichuan basin but relative small in east, suggesting a Moho dipping to the west.

[67] If the material of the Tibetan Plateau is extruded eastward [*Tapponnier et al.*, 1982], the Sichuan basin is clearly an important boundary and the above observations suggest strong interaction between the Tibetan Plateau and the Sichuan basin. Basins can be classified as rift (extensional) basins, which subside due to extensional thinning, followed by thermal cooling subsidence, and flexural basins, which is developed by loading by thrust sheets in a compressional regime [*Watson et al.*, 1987]. It is believed that the basins in western China are flexural and those in the east are extensional [*Watson et al.*, 1987]. Basins in the central China (including Sichuan) are more complex [*Korsch et al.*, 1997], but the Sichuan basin was considered to be a flexural basin by *Watson et al.* [1987]. A flexual basin tends to develop a wedge-shaped basin, thickening toward the thrust front [*Watson et al.*, 1987]. A wedge-shaped Sichuan basin with the wedge thickening toward the Longmen Shan thrust fault is clearly consistent with the change in the crustal thickness in the basin and the shift between the basin location and the high *Pn* velocity.

[68] Another scenario, which is highly speculative, is that when the plateau material moves eastward, hitting the relatively stable Sichuan basin, the material is channeled to the south; as a result of the eastward extrusion of the plateau, the upper crust of the Sichuan basin is pushed to the east, which explains the shift of the *Pn* fast anomaly relative to the surface location of the basin. This is possible, following the idea that the deformation of the plateau in the upper crust is decoupled from that of the lower crust, at least around the plateau margins [*Burchfiel and Royden*, 1991; *Royden et al.*, 1997]. However, this may be difficult because there is little evidence for significant E-W crustal shortening across the Longmen Shan and its adjacent foreland from geological and GPS data [*Burchfiel et al.*, 1995; *Chen et al.*, 2000].

[69] The complex pattern of station delays may be an indication that the whole crust (including the Moho) of the eastern margin of the Tibetan Plateau is highly deformed, just as the high deformation of the upper crust and the lower crust at the eastern margin that *Royden et al.* [1997] showed in a numerical simulation.

[70] The fast directions of *Pn* anisotropy beneath the plateau southeastern margin form a clear rotational pattern, from the E-W direction in east central Tibet, to the N-S direction in western Yunnan, to the E-W direction in southern Myanmar, and to the N-S direction in western Myanmar. The observation correlates with the results from geology [*Burchfiel and Wang*, 2003], GPS measurements [*Chen et al.*, 2000], and numerical modeling [*Royden et al.*, 1997] that suggest the crustal deformation in the southeastern margin of the plateau consists of a clockwise rotation of material around the eastern Himalayan syntaxis. The correlation seems to suggest a mantle lithospheric deformation of the similar style.

6. Conclusion

[71] 1. The *Pn* velocities of China are characterized by a mosaic of very fast and very slow anomalies. The *Pn* velocities are high beneath the major basins in the west (Sichuan, Qaidam, west Tarim, Tulufan, and Junggar). The *Pn* velocities are low in areas of active volcanoes (Myanmar and western Yunnan) and Quaternary volcanisms in northern Tibet, in seismically active areas in north China and Tien Shan, and in the southern part of south China (the Hainan plume).

[72] 2. The *Pn* anisotropy beneath most areas of the major basins in the west are less than 1%. Strong anisotropy is found beneath high-deformation regions (the Tibetan Plateau, southeastern margin of the Tibetan Plateau, western Tien Shan, and part of north China), suggesting the anisotropy is likely related to recent mantle deformation and large-scale tectonic activities.

[73] 3. Crustal thickness inferred from our station delays are consistent with previous models, which correlate well with surface topography.

[74] 4. A large area of north China shows prominent low *Pn* velocities beneath the Archean basement. The crust there is the thinnest of China. The thinnest crust is located in north China and Songliao basins. Our observations are consistent with rifting, lithospheric thinning, and mantle upwelling in the region. The *Pn* anisotropy is consistent with a dextral simple shear in the NNE direction in the lithosphere mantle during the last (and ongoing) major deformation period.

[75] 5. Our model in Tibet shows low *Pn* velocity in the north and high velocity in the south in general, consistent with previous studies. However, significant fine structures exist. Southern Tibet has significant E-W structure. Low-velocity anomalies can be traced from northern Tibet across southwestern Tibet and south central Tibet to the India plate. Anisotropy is absent beneath much of the Himalaya block, but consistent anisotropy with E-W fast direction is present beneath the Lhasa block and large anisotropy (up to 4%) is observed in low-velocity regions of northern and western Tibet. Station delays in the eastern margin suggest that the whole crust is likely highly deformed. The anisotropy

pattern in the southeastern margin suggests a mantle lithospheric deformation similar to the clockwise rotation of material observed at the surface.

Appendix A: A Source Selection Method Used in This Study

[76] To reduce uneven distribution of earthquakes, we adopt the following procedure to select events. The procedure aims to locate earthquake clusters and then choose the event with most number of observations in a cluster and discard all the other events in that cluster. (1) Get one event as the center of the first group. (2) Calculate the distance between the second event and the first group, say d_{21}. If $d_{21} > d_{\min}$ (where $d_{\min}$ is given, depending on the earthquake density and the desired ray coverage), then the event is set to be the center of a new group (the second group), otherwise this event is grouped into the first group. (3) Calculate the distances between the ith event and the existing N groups; if the shortest distance is less than $d_{\min}$, then add this event to the group corresponding to the shortest distance with this event; otherwise the ith event is set to be the center of the $(N+1)$th group. (4) Go through all events by applying step 3. Finally all events are grouped into M groups. (5) Average the epicenters of all events in the same group, and use the averaged locations as the center of the group. Regroup all events so that the distance between the event and its corresponding group center is less than $d_{\min}$. For an event belonging to several groups, group it into the nearest group. As a result, some groups may be cancelled and some new groups will be added. (6) Repeat steps 4 and 5 until no groups are cancelled and no new group are added. Finally, we choose the event with the largest number of travel time picks in each group for our inversion. All the other events are discarded. The $d_{\min}$ used in this study is 8 km.

[77] **Acknowledgments.** We thank Walter Mooney, the Associate Editor, and an anonymous reviewer for constructive comments, which greatly improved the manuscript. We benefited from discussion with Wang-Ping Chen, Jonathan Lees, Rongsheng Zeng, Jieshou Zhu, Hongzheng Wang, Sitian Li, and Jianye Ren on early version of the manuscript. We thank Youshun Sun for a preprint of their paper. This work was partially supported by National Key Basic Research Program of China (G19998040702) and a William and Flora Hewlett International Research Grant.

References

Aki, K., and P. G. Richards (2002), *Quantitative Seismology*, 2nd ed., Univ. Sci. Books, Sausalito, Calif.

Arnaud, N. O., P. Vidal, P. Tapponnier, P. Matte, and M. Deng (1992), The high K_2O volcanism of northwestern Tibet: Geochemistry and tectonic implications, *Earth Planet. Sci. Lett.*, *111*, 351–367.

Backus, G. E. (1965), Possible forms of seismic anisotropy of the uppermost mantle under oceans, *J. Geophys. Res.*, *70*, 3429–3439.

Bamford, D. (1977), *Pn* velocity anisotropy in a continental uppermost mantle, *Geophys. J. R. Astron. Soc.*, *49*, 29–48.

Barazangi, M., and J. F. Ni (1982), Velocities and propagation characteristics of *Pn* and *Sn* waves beneath the Himalayan arc and Tibetan Plateau: Possible evidence for underthrusting of Indian continental lithosphere beneath Tibet, *Geology*, *10*, 179–185.

Barry, T. L., and R. W. Kent (1998), Cenozoic magmatism in Mongolia and the origin of central and East Asia basalts, in *Mantle Dynamics and Plate Interactions in East Asia Geodyn. Ser.*, vol. 27, edited by M. Flower, S. L. Chung, and C. H. Lo, pp. 347–364, AGU, Washington, D. C.

Bassin, C., G. Laske, and G. Masters (2000), The current limits of resolution for surface wave tomography in North America, *Eos Trans. AGU*, *81*(48), Fall Meet. Suppl., Abstract S12A-03.

Beckers, J., S. Y. Schwartz, and T. Lay (1994), The velocity structure of the crust and upper mantle under China from broad-band *P* and *PP* waveform analysis, *Geophys. J. Int.*, *119*, 574–594.

Beghoul, N., M. Barazangi, and B. L. Isacks (1993), Lithospheric structure of Tibet and western North America: Mechanisms of uplift and a comparative study, *J. Geophys. Res.*, *98*, 1997–2016.

Bourjot, L., and B. Romanowicz (1992), Crust and upper mantle tomography in Tibet using surface-waves, *Geophys. Res. Lett.*, *19*, 881–884.

Brandon, C., and B. Romanowicz (1986), A "no-lid" zone in the central Chang-Thang platform of Tibet: Evidence from pure path phase velocity measurements of long-period Rayleigh waves, *J. Geophys. Res.*, *91*, 6547–6564.

Bump, H. A., and A. F. Sheehan (1998), Crustal thickness variations across the northern Tien Shan from teleseismic receiver functions, *Geophys. Res. Lett.*, *25*, 1055–1058.

Burchfiel, B. C., and L. H. Royden (1991), Tectonics of Asia 50 years after the death of Argand, Emile, *Eclogae Geol. Helv.*, *84*, 599–629.

Burchfiel, B. C., and E. C. Wang (2003), Northwest-trending, middle Cenozoic, left-lateral faults in southern Yunnan, China, and their tectonic significance, *J. Struct. Geol.*, *25*(5), 781–792.

Burchfiel, B. C., Z. L. Chen, Y. P. Liu, and L. H. Royden (1995), Tectonics of the Longmen Shan and adjacent regions, central China, *Int. Geol. Rev.*, *37*, 661–735.

Chen, W. P., and P. Molnar (1975), Short-period Rayleigh wave dispersion across the Tibetan Plateau, *Bull. Seismol. Soc. Am.*, *65*, 1051–1057.

Chen, W. P., and P. Molnar (1981), Constraints on the seismic wave velocity structure beneath the Tibetan Plateau and their tectonic implications, *J. Geophys. Res.*, *86*, 5937–5962.

Chen, W. P., and P. Molnar (1983), Focal depths of intracontinental and intraplate earthquakes and their implications for the thermal and mechanical properties of the lithosphere, *J. Geophys. Res.*, *88*, 4183–4214.

Chen, W. P., and J. Nabelek (1988), Seismogenic strike-slip faulting and the development of the North China Basin, *Tectonics*, *7*(5), 975–989.

Chen, W. P., and S. Ozalaybey (1998), Correlation between seismic anisotropy and Bouguer gravity anomalies in Tibet and its implications for lithospheric structures, *Geophys. J. Int.*, *135*, 93–101.

Chen, Y. H., S. W. Roecker, and G. L. Kosarev (1997), Elevation of the 410 km discontinuity beneath the central Tien Shan: Evidence for a detached lithospheric root, *Geophys. Res. Lett.*, *24*, 1531–1534.

Chen, Z., et al. (2000), Global Positioning System measurements from eastern Tibet and their implications for India/Eurasia intercontinental deformation, *J. Geophys. Res.*, *105*, 16,215–16,227.

Curtis, A., et al. (1998), Eurasian fundamental mode surface wave phase velocities and their relationship with tectonic structures, *J. Geophys. Res.*, *103*, 26,919–26,947.

Deng, W. (1978), Preliminary study on the petrology and petrochemistry of the Quaternary volcanic rocks, northern Tibetan Autonomous Region, *Acta Geol. Sin.*, *52*, 148–152.

Dricker, I. G., and S. W. Roecker (2002), Lateral heterogeneity in the upper mantle beneath the Tibetan Plateau and its surroundings from *SS-S* travel time residuals, *J. Geophys. Res.*, *107*(B11), 2305, doi:10.1029/2001JB000797.

England, P., and G. Houseman (1986), Finite strain calculations of continental deformation: 2. Comparison with the India-Asia collision zone, *J. Geophys. Res.*, *91*, 3664–3676.

Fan, G. W., and T. Lay (1998), Regionalized versus single-station waveguide effects on seismic discriminants in western China, *Bull. Seismol. Soc. Am.*, *88*, 1260–1274.

Gao, S. R. L., et al. (2002), Re-Os evidence for replacement of ancient mantle lithosphere beneath the north China craton, *Earth Planet. Sci. Lett.*, *198*, 307–322.

Gilder, A. A., G. R. Keller, L. Ming, and P. C. Goodell (1991), Timing and spatial-distribution of rifting in China, *Tectonophysics*, *197*, 225–243.

Grand, S. P., R. D. van der Hilst, and S. Widiyantoro (1997), Global seismic tomography: A snapshot of convection in the Earth, *GSA Today*, *7*(4), 1–7.

Griffin, W. L., A. D. Zhang, S. Y. O'Reilly, and C. G. Ryan (1998), Phanerozoic evolution of the lithosphere beneath the Sino-Korean craton, in *Mantle Dynamics and Plate Interactions in East Asia*, *Geodyn. Ser.*, vol. 27, edited by M. Flower, S. L. Chung, and C. H. Lo, pp. 107–126, AGU, Washington, D. C.

Griot, D. K., J. P. Montagner, and P. Tapponnier (1998), Phase velocity structure from Rayleigh and Love waves in Tibet and its neighboring regions, *J. Geophys. Res.*, *103*, 21,215–21,232.

Hartse, H. E., et al. (1997), A preliminary study of regional seismic discrimination in central Asia with emphasis on western China, *Bull. Seismol. Soc. Am.*, *87*, 551–568.

Hearn, T. M. (1996), Anisotropy *Pn* tomography in the west United States, *J. Geophys. Res.*, *101*, 8403–8414.

Hearn, T. M., and J. F. Ni (1994), *Pn* velocities beneath continental collision zones: The Turkish-Iranian Plateau, *Geophys. J. Int.*, *117*, 273–283.
Holt, W. E., and T. C. Wallace (1990), Crustal thickness and upper mantle velocities in the Tibetan plateau region from the inversion of regional *Pnl* waveforms: Evidence for a thick upper mantle lid beneath southern Tibet, *J. Geophys. Res.*, *95*, 12,499–12,525.
Houseman, G. A., D. P. McKenzie, and P. Molnar (1981), Convective instability of a thickened boundary layer and its relevance for the thermal evolution of continental convergent belts, *J. Geophys. Res.*, *86*, 6115–6132.
Huang, J., D. Zhao, and S. Zheng (2002), Lithospheric structure and its relationship to seismic and volcanic activity in southwest China, *J. Geophys. Res.*, *107*(B10), 2255, doi:10.1029/2000JB000137.
Huang, Z., W. Su, Y. Peng, Y. Zheng, and H. Li (2003a), Rayleigh wave tomography of China and adjacent regions, *J. Geophys. Res.*, *108*(B2), 2073, doi:10.1029/2001JB001696.
Huang, J. L., X. D. Song, and S. Y. Wang (2003b), Fine structure of uppermost mantle Pn velocity beneath Sichuan-Yunnan area (in Chinese), *Sci. China, Ser. D*, *33*, 144–150.
Korsch, R. J., H. Z. Mai, Z. C. Sun, and J. D. Gorter (1997), Evolution and subsidence history of the Sichuan Basin, Southwest China, in *Basin Analysis, Global Sedimentary Geology and Sedimentology*, edited by B. J. Liu and S. T. Li, *Proc. Int. Geol. Congr.*, *30th*(8), 208–221.
Lebedev, S., and G. Nolet (2003), Upper mantle beneath Southeast Asia from *S* velocity tomography, *J. Geophys. Res.*, *108*(B1), 2048, doi:10.1029/2000JB000073.
Lees, J. M., and R. S. Crosson (1989), Tomographic inversion for three-dimensional velocity structure at Mount St. Helens using earthquake data, *J. Geophys. Res.*, *94*, 5716–5728.
Lei, J. S., H. L. Zhou, and D. P. Zhao (2002), 3-D velocity structure of *P*-wave in the crust and upper-mantle beneath Pamir and adjacent region, *Chin. J. Geophys.*, *45*(6), 852–861.
Leveque, J. J., L. Rivera, and G. Wittlinger (1993), On the use of the checker-board test to assess the resolution of tomographic inversions, *Geophys. J. Int.*, *115*, 313–318.
Li, S. L., and W. D. Mooney (1998), Crustal structure of China from deep seismic sounding profiles, *Tectonophysics*, *288*, 105–113.
Li, S. T., X. X. Mo, and S. Yang (1995), Evolution of circum-Pacific basins and volcanic belts in east China and their geodynamic setting, *J. China Univ. Geosci.*, *8*(1), 4–10.
Li, Z. X. (1998), Tectonic history of the major east Asia lithospheric blocks since the mid-Proterozoic: A synthesis, in *Mantle Dynamics and Plate Interactions in East Asia*, *Geodyn. Ser.*, vol. 27, edited by M. F. J. Flower et al., pp. 221–243, AGU, Washington, D. C.
Liu, F. T., and A. Jin (1993), Seismic tomography of China, in *Seismic Tomography Theory and Practice*, edited by H. M. Iyer and K. Hirahara, pp. 299–318, Chapman and Hall, New York.
Liu, F. T., et al. (1990), 3-D velocity images beneath the Chinese continent and adjacent regions, *Geophys. J. Int.*, *101*, 379–394.
Liu, G. (1987), The Cenozoic rift system of the North China Plain and the deep internal process, *Tectonophysics*, *133*, 277–285.
Lyon-Caen, H. (1986), Comparison of the upper mantle shear wave velocity structure of the Indian shield and the Tibetan Plateau and tectonic implications, *Geophys. J. R. Astron. Soc.*, *86*, 727–749.
Ma, X. G., G. D. Liu, and J. Su (1984), The structure and dynamics of the continental lithosphere in north-northeast China, *Ann. Geophys.*, *2*(6), 611–620.
Ma, Z. J., et al. (1990), *Earthquake Prediction: Nine Major Earthquakes in China*, Springer-Verlag, New York.
Mahdi, H., and G. L. Pavlis (1998), Velocity variations in the crust and upper mantle beneath the Tien Shan inferred from Rayleigh wave dispersion: Implications for tectonic and dynamic processes, *J. Geophys. Res.*, *103*, 2693–2703.
McNamara, D. E., T. J. Owens, P. G. Silver, and F. T. Wu (1994), Shear wave anisotropy beneath the Tibetan Plateau, *J. Geophys. Res.*, *99*, 13,655–13,665.
McNamara, D. E., T. J. Owens, and W. R. Walter (1995), Observations of regional phase propagation across the Tibetan Plateau, *J. Geophys. Res.*, *100*, 22,215–22,229.
McNamara, D. E., W. R. Walter, T. J. Owens, and C. J. Ammon (1997), Upper mantle velocity structure beneath Tibetan Plateau from *Pn* travel time tomography, *J. Geophys. Res.*, *102*, 493–505.
Menzies, M. A., and Y. G. Xu (1998), Geodynamics of the north China craton, in *Mantle Dynamics and Plate Interactions in East Asia*, *Geodyn. Ser.*, vol. 27, edited by M. F. J. Flower et al., pp. 155–165, AGU, Washington, D. C.
Molnar, P., and P. Tapponnier (1975), Cenozoic tectonics of Asia: Effects of a continental collision, *Science*, *189*, 419–426.
Molnar, P., P. England, and J. Martinod (1993), Mantle dynamics, uplift of the Tibetan Plateau, and the Indian monsoon, *Rev. Geophys.*, *31*, 357–386.
Nelson, K. D., et al. (1996), Partially molten middle crust beneath southern Tibet: Synthesis of project INDEPTH results, *Science*, *274*, 1684–1688.
Ni, J. F., and M. Barazangi (1983), High frequency seismic wave propagation beneath the Indian shield, Himalayan arc, Tibetan Plateau and surrounding regions: High uppermost mantle velocities and efficient propagation beneath Tibet, *Geophys. J. R. Astron. Soc.*, *72*, 665–689.
Nicolas, A., and N. I. Christensen (1987), Formation of anisotropy in upper mantle peridotite, in *Composition, Structure and Dynamics of the Lithosphere-Asthenosphere System*, vol. 16, edited by K. Fuchs and C. Froidevaux, pp. 111–123, AGU, Washington, D. C.
Nolet, G. (Ed.) (1987), *Seismic Tomography: With Application in Global Seismology and Exploration Geophysics*, D. Reidel, Norwell, Mass.
Northrup, C. J., L. H. Royden, and B. C. Burchfiel (1995), Motion of the Pacific plate relative to Eurasia and its potential relation to Cenozoic extension along the eastern margin of Eurasia, *Geology*, *23*, 719–722.
Paige, C. C., and M. A. Saunders (1982a), LSQR: An algorithm for sparse linear equations and least squares problems, *ACM Trans. Math. Software*, *8*(1), 43–71.
Paige, C. C., and M. A. Saunders (1982b), LSQR: Sparse linear equations and least squares problems, *ACM Trans. Math. Software*, *8*(2), 195–209.
Patton, H. (1980), Crustal and upper mantle structure of the Eurasian continent from the phase velocity and *Q* of surface waves, *Rev. Geophys.*, *18*, 605–625.
Pei, S. P., et al. (2002), *Pn* velocity tomography of Xinjiang, China and adjacent region, *Chin. J. Geophys.*, *45*(2), 217–224.
Phillips, W., H. Hartse, S. Taylor, and G. Randall (2000), 1 Hz *Lg Q* tomography in central Asia, *Geophys. Res. Lett.*, *27*, 3425–3428.
Phillips, W. S., G. E. Randall, and S. R. Taylor (1998), Path correction using interpolated amplitude residuals: An example from central China, *Geophys. Res. Lett.*, *25*, 2729–2732.
Rapine, R. R., J. F. Ni, and T. M. Hearn (1997), Regional wave propagation in China and its surrounding regions, *Bull. Seismol. Soc. Am.*, *87*, 1622–1636.
Ren, J. Y., et al. (2002), Late Mesozoic and Cenozoic rifting and its dynamic setting in eastern China and adjacent areas, *Tectonophysics*, *344*(3–4), 175–205.
Ribe, N. M. (1992), On the relation between seismic anisotropy and finite strain, *J. Geophys. Res.*, *97*, 8737–8747.
Ritzwoller, M. H., and A. L. Levshin (1998), Eurasian surface wave tomography: Group velocities, *J. Geophys. Res.*, *103*, 4839–4878.
Rodgers, A. J., and S. Y. Schwartz (1998), Lithospheric structure of the Qiangtang Terrain, northern Tibetan Plateau, from complete regional waveform modeling: Evidence for partial melt, *J. Geophys. Res.*, *103*, 7137–7152.
Roecker, S., T. Sabitova, L. Vinnik, Y. Burmakov, M. Golvanov, R. Mamatkanova, and L. Munirova (1993), Three-dimensional elastic wave velocity structure of the western and central Tien Shan, *J. Geophys. Res.*, *98*, 15,779–15,796.
Rowley, D. B. (1996), Age of initiation of collision between India and Asia: A review of stratigraphic data, *Earth Planet. Sci. Lett.*, *145*, 1–13.
Royden, L. H., et al. (1997), Surface deformation and lower crustal flow in eastern Tibet, *Science*, *276*, 788–790.
Sandvol, E., J. Ni, R. Kind, and W. Zhao (1997), Seismic anisotropy beneath the southern Himalayas–Tibet collision zone, *J. Geophys. Res.*, *102*, 17,813–17,824.
Silver, P. G. (1996), Seismic anisotropy beneath the continents: Probing the depths of geology, *Annu. Rev. Earth Planet. Sci.*, *24*, 385–432.
Sun, Y. S., X. Li, S. Kuleli, F. D. Morgan, and M. N. Toksoz (2004), Adaptive moving window method for 3–D P-velocity tomography and its application in China, *Bull. Seismol. Soc. Am.*, *94*, 740–746.
Tapponnier, P., et al. (1982), Propagating extrusion tectonics in Asia: New insights from simple experiments with plasticine, *Geology*, *10*, 611–616.
Teng, J. W., Q. S. Wang, Y. L. Liu, and S. Y. Wei (1983), Geophysical field characteristics, distribution and formation of hydrocarbon-bearing basins of east China (in Chinese), *Chin. J. Geophys.*, *26*(4), 319–330.
Tichelaar, B. W., and L. J. Ruff (1989), How good are our best models? Jackknifing, bootstrapping, and earthquake depth, *Eos Trans. AGU*, *70*(20), 605–606.
Turner, S., et al. (1993), Timing of the Tibetan uplift constrained by analysis of volcanic rocks, *Nature*, *364*, 50–54.
van der Hilst, R. D., S. Widiyantoro, and E. R. Engdahl (1997), Evidence for deep mantle circulation from global tomography, *Nature*, *386*, 578–584.
Van der Sluis, A., and H. A. van der Vorst (1987), Numerical solution of large, sparse linear algebraic systems arising from tomographic problems, in *Seismic Tomography: With Applications in Global Seismology and Exploration Geophysics*, edited by G. Nolet, pp. 49–83, D. Reidel, Norwell, Mass.
Wang, H. Z., and X. X. Mo (1995), An outline of the tectonic evolution of China, *Episodes*, *18*, 6–16.

Wang, Q., et al. (2001), Present-day crustal deformation in China constrained by global positioning system measurements, *Science*, *294*, 574–577.

Wang, S. Y., et al. (2002), Velocity structure of uppermost mantle beneath China continent from *Pn* tomography, *Sci. China, Ser. D*, *45*(2), 143–150.

Watson, M., A. B. Hayward, D. N. Parkinson, and Z. M. Zhang (1987), Plate tectonic history, basin development and petroleum source rock deposition onshore China, *Mar. Pet. Geol.*, *4*, 205–225.

Wolfe, C. J., and F. L. Vernon (1998), Shear-wave splitting at central Tien Shan: Evidence for rapid variation of anisotropic patterns, *Geophys. Res. Lett.*, *25*, 1217–1220.

Wu, F. T., A. L. Levshin, and V. M. Kozhevnikov (1997), Rayleigh wave group velocity tomography of Siberia, China and the vicinity, *Pure Appl. Geophys.*, *149*, 447–473.

Xie, J. K., and H. J. Patton (1999), Regional phase excitation and propagation in the Lop Nor region of central Asia and implications for *P*/*Lg* discriminants, *J. Geophys. Res.*, *104*, 941–954.

Xu, G. M., et al. (2000), The 3–D structure of shear waves in the crust and mantle of east continental China inverted by Rayleigh wave data, *Chin. J. Geophys.*, *43*(3), 395–406.

Xu, P., F. Liu, Q. Wang, B. Cong, and H. Chen (2001), Slab-like high velocity anomaly in the uppermost mantle beneath the Dabie-Sulu orogen, *Geophys. Res. Lett.*, *28*, 1847–1850.

Xu, Y., F. Liu, J. Liu, and H. Chen (2002), Crust and upper mantle structure beneath western China from *P* wave travel time tomography, *J. Geophys. Res.*, *107*(B10), 2220, doi:10.1029/2001JB000402.

Yin, A., and T. M. Harrison (2000), Geological evolution of the Himalayan-Tibetan orogen, *Annu. Rev. Earth Planet. Sci.*, *28*, 211–280.

Zelt, C. A. (1998), Lateral velocity resolution from three-dimensional seismic refraction data, *Geophys. J. Int.*, *135*, 1101–1112.

Zeng, R. S., C. Y. Wang, and D. N. Zhang (1995a), On the dynamics of extensional basin, *Pure Appl. Geophys.*, *145*, 579–603.

Zeng, R. S., Z. F. Ding, and Q. J. Wu (1995b), A review on the lithospheric structures in the Tibetan Plateau and constraints for dynamics, *Pure Appl. Geophys.*, *145*, 425–443.

Zhang, Y. S., and T. Lay (1996), Global surface wave phase velocity variations, *J. Geophys. Res.*, *101*, 8415–8436.

Zhang, Z. M., J. G. Liou, and R. G. Coleman (1984), An outline of the plate tectonics of China, *Geol. Soc. Am. Bull.*, *95*, 295–312.

Zhao, L. S., and J. K. Xie (1993), Later variation in compressional velocities beneath the Tibetan Plateau from *Pn* traveltime tomography, *Geophys. J. Int.*, *115*, 1070–1084.

Zhao, L. S., D. V. Helmberger, and D. G. Harkrider (1991), Shear-velocity structure of crust and upper mantle beneath the Tibet Plateau and southeastern China, *Geophys. Int. J.*, *105*, 713–730.

Zhu, J. S., et al. (2002), High resolution surface wave tomography in east Asia and west Pacific marginal seas, *Chin. J. Geophys.*, *45*(5), 679–698.

Zhu, L., D. V. Helmberger, C. K. Saikia, and B. B. Woods (1997), Regional waveform calibration in the Pamir-Hindu Kush region, *J. Geophys. Res.*, *102*, 22,799–22,813.

C. Liang and X. Song, Department of Geology, University of Illinois at Urbana-Champaign, Urbana, IL 61891, USA. (xsong@uiuc.edu)

J. Huang, Center of Analysis and Prediction, China Seismological Bureau, P.O. Box 166, Beijing 1000036, China.